Master's Thesis in Condensed Matter Physics

Generating small magnetic fields inside an open-end magnetic shielding with a superconducting solenoid magnet

Lukas Maximilian Vogl

Walter-Meißner-Institut der Bayerischen Akademie der Wissenschaften
Physik-Department, TUM School of Natural Science, Technische Universität München

Master's Thesis in Condensed Matter Physics

Generating small magnetic fields inside an open-end magnetic shielding with a superconducting solenoid magnet

Author: Lukas Maximilian Vogl
Supervisor: Prof. Dr. Rudolf Gross
Advisor: Dr. Nadezhda Kukharchyk
Submission Date: 23 May 2023

Abstract

Quantum memory is an essential part for the development in the quantum information field.

One of the most promising realisation of quantum memories has been demonstrated for storage of optical photons in rare-earth-doped crystals, reaching a storage time of 6 hours [15]. Such long storage times have been achieved due to, working at the zero first-order Zeeman shift point (ZEFOZ). At this point the phase-sensitivity of a spin system to the magnetic field fluctuations is strongly reduced, and thus longer coherence times can be achieved. Such ZEFOZ transitions are present in the hyperfine states of rare earth ions close to zero magnetic fields, which enables the design of quantum memories compatible with the zero-field environments required for superconducting quantum computing circuits. Here, we present a setup for a highly controllable homogeneous magnetic environment with additional shielding from external background magnetic fields. This environment should allow for precise control of the magnetic field at the sample position, fine tuning to the ZEFOZ transitions, and additional protection of the superconducting quantum circuits from the fields applied to the rare earth ion spins.

I will first show a mathematical comparison of the magnetic field distribution of a Helmholtz coil, a plain solenoid and my improved solenoid. Then, I use a simulation to show how a magnetic shield can be used to shield the generated field and how it influences the field homogeneity of the improved solenoid. Based on this findings, I will construct a superconducting solenoid and a magnetic shield, install it in an dilution refrigerator and measure its performance.

Contents

1. Introduction

Every computer needs to be able to store information it is processing. In classical computers, the smallest unit of information is called a bit,which can have two states, on (1) or off (0). In quantum computers the smallest unit of information is called a quantum bit, short qubit. Qubits have a ground state and a excited state similar to the classical bit but it can exist in a superposition of both states. Additionally a qubit also has a phase. To be able to store this superposition of states, a quantum memory is needed.

Superposition is the mixing of two states, as example, the probability that a spin is pointing up or down encoded into one state. A quantum memory is able to store this information and present it later without collapsing the superposition.

For quantum memory, two level systems are used. The corresponding wave function representation with the ground state $|g\rangle$ and excited state $|e\rangle$, is given as $|\Psi\rangle = a(t)\,|g\rangle + b(t)\,|e\rangle$. The two complex functions $a(t)$ and $b(t)$ have to be normalized so $|a(t)|^2 + |b(t)|^2 = 1$. With this, all states can be visualized on the surface of a Bloch sphere and the wave function can be written as $|\Psi\rangle = \cos\left(\frac{\theta(t)}{2}\right)|e\rangle + e^{i\varphi(t)}\sin\left(\frac{\theta(t)}{2}\right)|g\rangle$. The Bloch angle $\theta(t)$ can be interpreted as the amplitude or energy of the system, in ensembles as the population and $\varphi(t)$ as the phase.

A change the phase $\varphi(t)$ dose not change the energy of the quantum state, but dose change the quantum information encoded in it. Ensemble-based systems like an ensemble of rear-earth ions do suffer of a loss of signal intensity during dephasing. While there are methods like spin echo refocusing, the slower the dephasing in the first place is, the longer the quantum information can be stored. Dephasing in spin systems is mainly driven by fluctuations in the magnetic field, random spin flipping of nearby spins or other inhomogeneity's in the material. [10]

The dependence of the dephasing on the magnetic field fluctuation can be reduced by working at the zero first-order Zeeman shift (ZEFOZ) point. The Zeeman effect is the splitting of energy levels of electrons at the presence of a magnetic field. At the ZEFOZ point, the first derivative of the magnetic field dependence is zero, therefore the transition is protected from small fluctuations of the magnetic field.

Providing a stable, controllable magnetic environment, such that the ZEFOZ effect can be used in the rear-earth spin ensembles located in the same cryostat as a superconducting qubit setup, without influencing the later ones, is the goal of this thesis.

This will be achieved by a superconducting solenoid for precise generation of a magnetic field and a magnetic shield to shield the neighbouring qubit from the generated magnetic field.

2. Generation of magnetic fields

In general, there are two ways to generate a magnetic field: either with a permanent magnet or with an electric current. Since we want to control the field strength, permanent magnets are not suitable. In this chapter, I will discuss the generation of the magnetic fields and compare three different solenoid designs mathematically.
Since we are only interested in static fields, we can start with Biot-Savart's law for a constant electric current I along the path C given as

$$B(\boldsymbol{x}) = \frac{\mu_0 I}{4\pi} \int_C dl \times \frac{\boldsymbol{x} - l}{|\boldsymbol{x} - l|^3} \tag{2.1}$$

where μ_0 is the permeability of vacuum [6].

General solutions for Equation 2.1 for arbitrary current paths include non-analytical solvable elliptical integrals. But for current paths with a high degree of symmetry analytical solutions can exist along the symmetry axis.

2.1. Analytical calculation of the magnetic field

Figure 2.1 schematically shows the geometry for a Helmholtz coil, a plain solenoid and an improved solenoid design with additional windings at the top and bottom end of the plain solenoid. For these three geometries, analytical solution along the center axis exist. Approximating the Helmholtz coil with two rings with an point-like cross section and radius R, the field in z-direction along the center axis is given by

$$B_{z,helmholtz}(z) = \frac{\mu_0 I_{total}}{2} \left(\frac{R^2}{\sqrt{R^2 + (z - R/2)^2}^3} - \frac{R^2}{\sqrt{R^2 + (z + R/2)^2}^3} \right) \tag{2.2}$$

with $I_{total} = I_0 N$ being the total current in each ring and μ_0 the permeability of vacuum [7].

The simple solenoid can be approximated as an infinitely thin cylinder with radius R and length L, since R, L are large compared to the diameter of the wire we will be using. The field along the center can then be given as

$$B_{z,plain}(z) = \frac{\mu_0 I_0 N}{2L} \left(\frac{z + L/2}{\sqrt{R^2 + (z + L/2)^2}} - \frac{z - L/2}{\sqrt{R^2 + (z - L/2)^2}} \right) \tag{2.3}$$

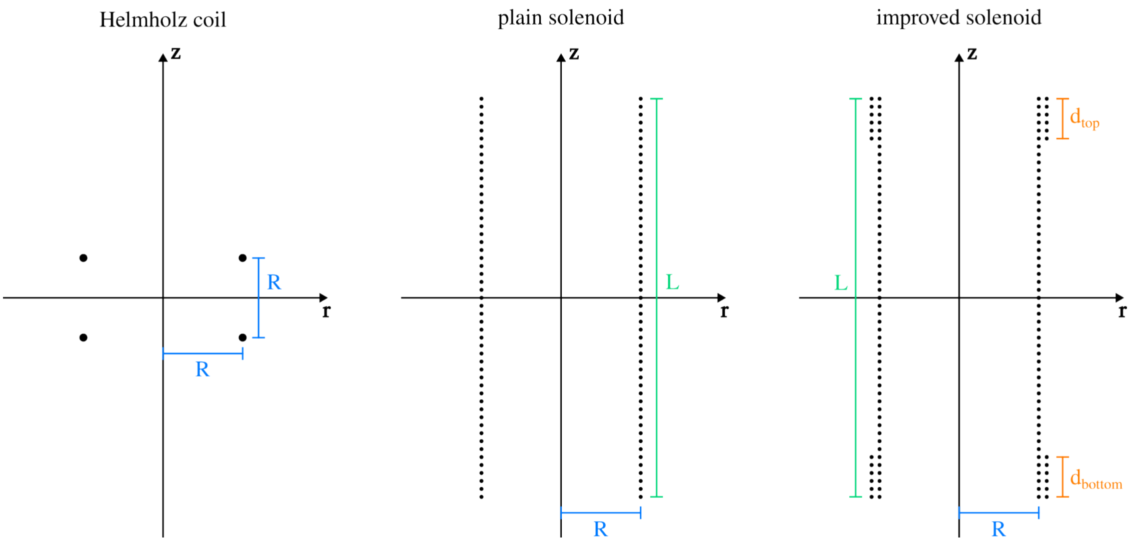

Figure 2.1.: The Helmholtz coil consists of two rings of radius R separated by distance R. The plain solenoid is a cylindrical coil with length L and radius R. The improved solenoid is an cylindrical coil with length L, radius R and additional layer of windings of a length d_{top} on the top end and d_{bottom} on the bottom end.

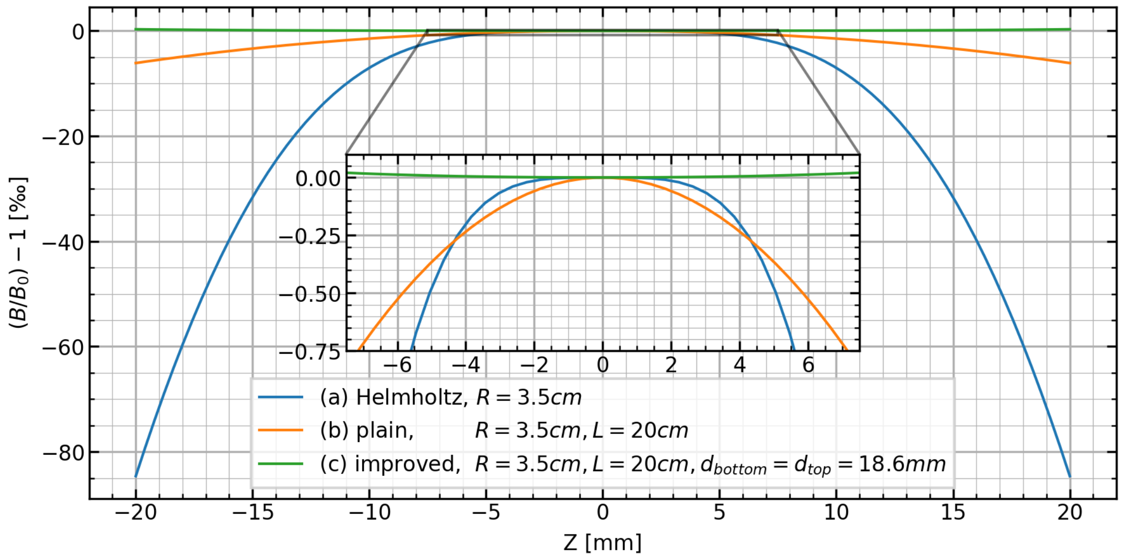

Figure 2.2.: Magnetic field distribution for the analytical approach. Normalized to the center along the z-axis for the solenoids shown in Figure 2.1. (a) is the Helmholtz coil with with a radius of 3.5 cm. (b) is the plain solenoid with the same radius and a length of 20 cm. (c) is the improved solenoid with $d_{bottom} = d_{top} = 18.6$ mm.

with I_0 being the current inside the wire and N the total number of windings [5].

The special characteristic of Helmholtz coils is that the first and second order derivatives are zero at the centre position, which can be seen in Figure 2.2 (a). With this property, the Helmholtz coil has a higher uniformity for a small region around $z = 0$ compared to the plain solenoid, but for $|z| > 4\,\text{mm}$, the plain solenoid provides a better uniformity.

Since I wanted to maximize the volume of high field uniformity even further, I came up with the improved solenoid by adding additional windings at the top and bottom as depicted in Figure 2.1. The field for the improved solenoid can be calculated by dividing the solenoid in three sections, a plain solenoid and two additional solenoids on the ends, and using Equation 2.3 for each:

$$\begin{aligned} B_{z,mod}(r,z) = & B_{z,plain}(z)|_{L=L_0} \\ & + B_{z,plain}(z + \frac{L_0 - d_{top}}{2})|_{L=d_{top}} \\ & + B_{z,plain}(z - \frac{L_0 - d_{bottom}}{2})|_{L=d_{bottom}}. \end{aligned} \tag{2.4}$$

Here, L_0 is the total length of the solenoid, shown in Figure 2.1 as L.

This improved design in free space gives us for $d_{top} = d_{bottom} = 18.6\,\text{mm}$ a nearly perfectly uniform field.

2.2. Numerical calculation of the magnetic field

As mentioned before, to calculate the field in radial direction, no analytically solvable solution exists. We can never the less numerically calculate the fields, since complete elliptical integrals of first, second and third order,which appear in the solution, are implemented in the C/C++ standard library. With this, we can use the solution from T. Tang [12] for the current density

$$J = \frac{I}{L}\delta(r - R)(-\sin\phi, \cos\phi, 0), \qquad z \in \left(-\frac{L}{2}, \frac{L}{2}\right): \tag{2.5}$$

$$B_r(r,z) = \frac{\mu_0 I}{2\pi L}\sqrt{\frac{R}{r}}\left[\frac{k^2-2}{k}K(k^2) + \frac{2}{k}E(k^2)\right]_{\zeta_-}^{\zeta_+}, \tag{2.6}$$

$$B_z(r,z) = \frac{\mu_0 I}{2\pi L}\frac{1}{2\sqrt{Rr}}\left[\zeta k\left(K(k^2) + \frac{R-r}{R+r}\Pi(h^2,k^2)\right)\right]_{\zeta_-}^{\zeta_+} \tag{2.7}$$

with

$$h^2 = \frac{4Rr}{(R+r)^2}, \qquad k^2 = \frac{4Rr}{(R+r)^2 + \zeta^2}, \qquad \zeta_\pm = z \pm \frac{L}{2} \tag{2.8}$$

and $K(m)$, $E(m)$ and $\Pi(n,m) = \Pi(n, \frac{\pi}{2}, m)$ the Legendre complete elliptical integrals of first, second and third kind.

The absolute field strength is given by:

$$B(r,z) = \sqrt{B_r(r,z)^2 + B_z(r,z)^2} \tag{2.9}$$

The Helmholtz coil is calculated as a composition of 2 very short solenoids:

$$B_{r/z,helmholtz}(r,z) = B_{r/z}(r, z - R/2)|_{L<<R} + B_{r/z}(r, z + R/2)|_{L<<R} \tag{2.10}$$

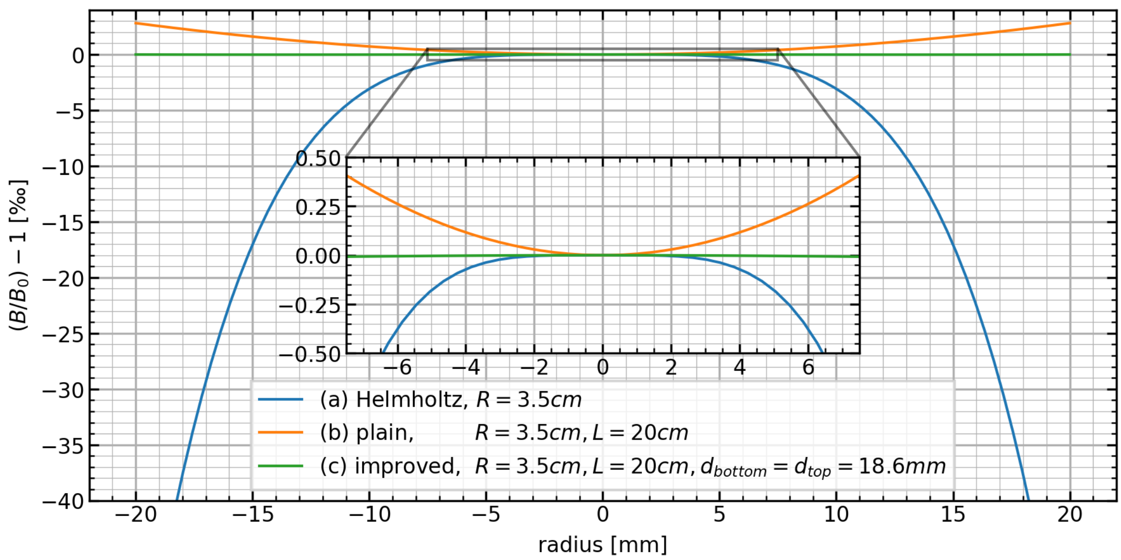

Figure 2.3.: Magnetic field distribution for the numerical approach. Normalized to the center along the r-axis at $z = 0$ for the solenoids shown in Figure 2.1. (a) is the Helmholtz coil with with a radius of 3.5 cm. (b) is the plain solenoid with the same radius and a length of 20 cm. (c) is the improved solenoid with $d_{bottom} = d_{top}$= 18.6 mm.

The result for the radial direction is shown in Figure 2.3, similar to the axial case in Figure 2.2, the Helmholtz coil has a plateau at $r = 0$ and is better than the plain solenoid for a small region around the center. Outside of this region, the plain solenoid outperforms the Helmholtz coil. The improved solenoid shows now visible deviation in field strength and outperforms both the Helmholtz coil and the plain solenoid.

Looking at the cross-sectional view of field strength at the center in the z-r-plane of the solenoids, the light green area in Figure 2.4 shows the area where the field strength deviates less than 1‰ from the center field strength at $z = r = 0$. One can clearly see, how the improved solenoid has a significantly higher magnetic field uniformity, in both axial and radial direction, than any of the other two.

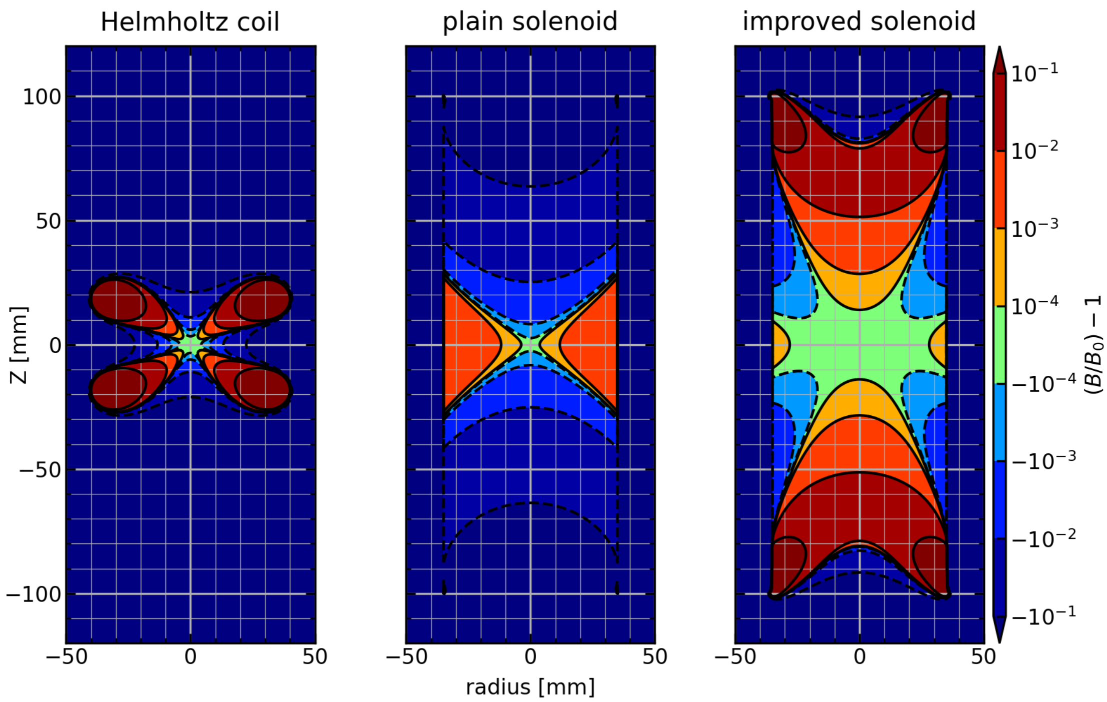

Figure 2.4.: Contour graph for each magnet design. The coloured areas show the deviation of the field strength from the center at $z = r = 0$ in discrete steps.

For geometries with strong symmetry, we can find solutions, describing the system, which can be expressed with numerical equations. When increasing the complexity of the system further, we need to use numerical simulations. In chapter 4, I will use numerical simulation to evaluate the magnetic field of the improved solenoid inside a magnetic shield with high permeability.

2.3. Flux trapping in superconducting solenoids

When constructing superconducting solenoids, flux trapping inside of the superconductor has to be considered. NbTi is a type II superconductor, meaning that even without defects inside the superconducting material, flux can enter the superconductor and get trapped.

Figure 2.5 shows different states of a superconducting solenoid after initial cool down. In Figure 2.5(a), the solenoid is first cooled down below critical temperature T_c and no flux is trapped. After we apply a current I_0, some field lines start to penetrate the superconductor,Figure 2.5(b), and after switching the current of in Figure 2.5(c), the flux lines remain trapped. We can see that the trapped field lines generate an field in the

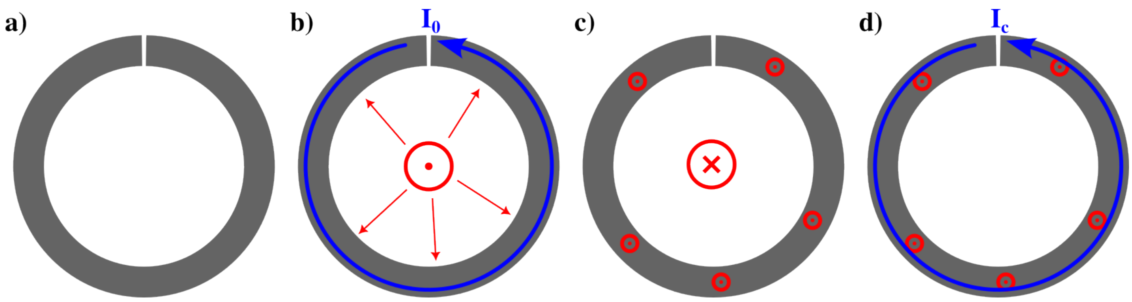

Figure 2.5.: Different states of an superconducting solenoid during its operation. See text for detailed description.

inverse direction than previously applied. To reach zero field inside the solenoid we need to apply a compensating current I_c shown in Figure 2.5(d).[13]
The bigger the correction area, exposed to the flux perpendicular to the surface, the bigger is this effect.

3. Suppression of magnetic fields

3.1. Permeability

The Permeability μ is a material specific property, describing how a material responses to magnetic fields:

$$B = \mu H \tag{3.1}$$

For classification, the relative permeability $\mu_r = \mu/\mu_0$ is used, with μ_0 being the permeability of vacuum.

Materials with $0 \leq \mu_r < 1$ are called diamagnetic, they want to expel the magnetic field from there volume and generate a magnetic field in the direction opposite to the externally applied field. A special case are type I superconductors, the have $\mu_r = 0$ and expel all of the field.

Materials with $1 < \mu_r$ are called paramagnetic. Most materials fall in this class, they respond weakly to magnetic fields, by concentrating the field in them.

Materials with $1 << \mu_r$ are called ferromagnetic. This materials can have a relative permeability up to $\mu_r \approx 10^5 - 10^6$. They strongly attract magnetic fields and are often used in transformers or as shielding materials.

μ-metals are of the last type, engineered to have a very hight permeability with good mechanical properties in an big temperature range.
While amorphous metals can have higher permeability than μ-metals, their poor mechanical properties often do not allow there use.

3.2. Shielding materials

We selected Cryophy as our shielding material for its good performance in cryogenic and low field strength environments. It contains 81% Ni, 5% Mo and 14% Fe [3].

Since the permeability of Cryophy is not constant over several orders of magnitudes of magnetic field strength, a BH-Curve is needed for accurate simulations, which is shown in Figure 3.1. A BH-Curve describes how the material responses at different field strengths. The blue curve is the measured data for an annealed muMetal® by Arpaia Et al.[1]. While the muMetal® and Cryophy are not identical in their composition, they should be similar enough to use the data from muMetal® for the simulation. Comsol[1] has several criteria for a good BH-curve resulting in valid simulations: The curve has to start from the Origin, it should be continues over it entire range, and needs a high smoothness [8]. For this purpose, Comsol as a built-in module to optimize any BH-curve on the mentioned criteria. The result of this tool is shown in orange in Figure 3.1. This was then used for all simulations.

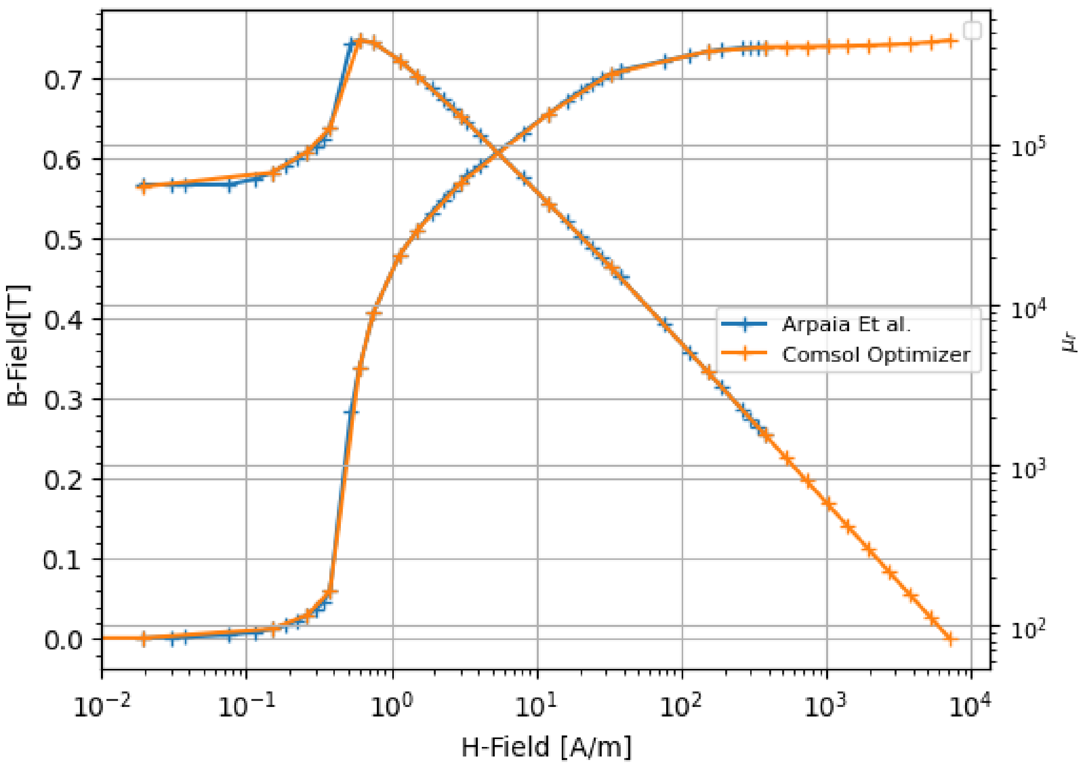

Figure 3.1.: B-field strength in dependence of H-field strength. Comsol simulations have several requirements for valid BH-curves. With the help of the ACDC Module "B-H curve checker" by Comsol an optimized curve was generated from the data from Arpaia Et al. [1]

3.3. Hysteresis of µ-metal

Due to the magnetic remanence of ferromagnetic materials, these materials experience hysteresis. How strong the hysteresis is, depends on the material and the maximal magnetic field it was exposed to. Figure 3.2 shows the hysteresis loops for two samples measured in [1]. Sample 1 is annealed after final fabrication, reflecting the fabrication process for our shields.

[1] see chapter 4

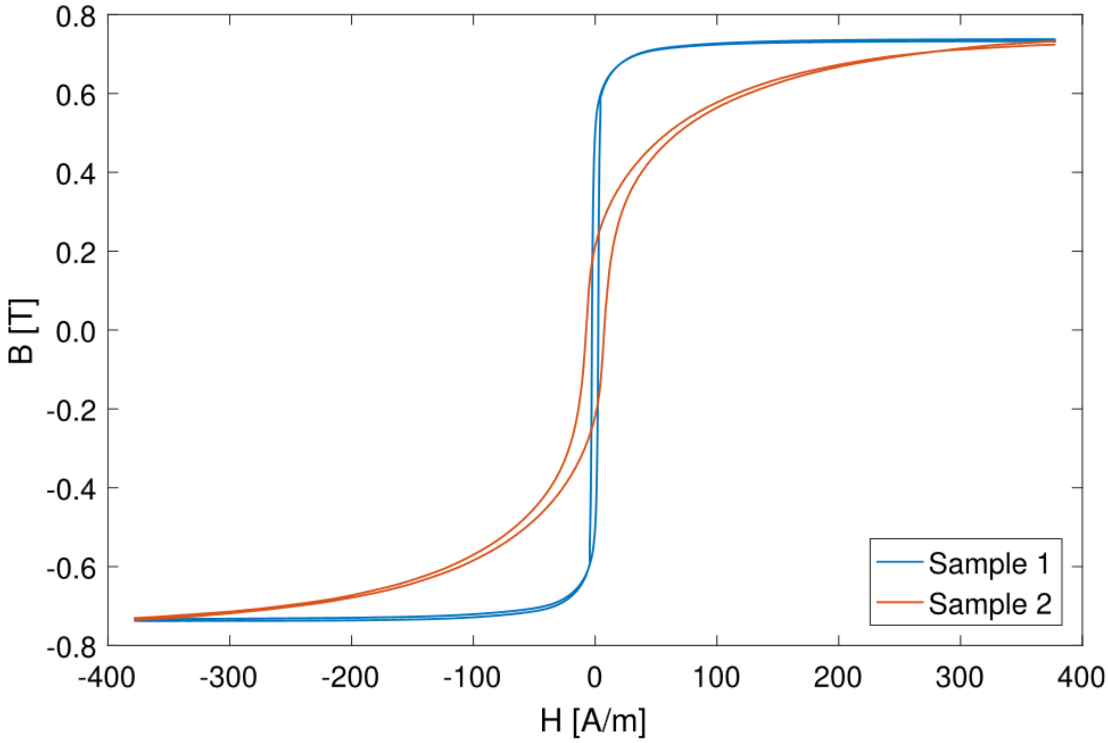

Figure 3.2.: DC hysteresis loops measured by [1]. Sample 1 is annealed after fabrication, sample 2 was not annealed.

Sample 2 is not annealed after final fabrication.
The coercive field for sample 1 is $1.27\,\frac{\mathrm{A}}{\mathrm{m}}$ and for sample 2 is $6.89\,\frac{\mathrm{A}}{\mathrm{m}}$, equivalent to $1.60\,\mu\mathrm{T}$ and $8.66\,\mu\mathrm{T}$ in vacuum respectively. The coercive field is the field required to demagnetize the material. From this we should expect a very small hysteresis at our operational amplitude of $\pm 50\,\mathrm{mT}$.

4. Designing and modeling

4.1. Design requirements

The final design has to fulfill several requirements, given by the space restrictions in the cryostat and required magnetic performance:

The total length of the complete setup beneath the mixing chamber plate should not exceed 300 mm, in order to not interfere with the thermal shielding of the cryostat.
The total diameter should be as small as possible to minimize the footprint.
The field homogeneity should be in the order of 0.1‰ deviation inside a volume of $1\,\mathrm{cm}^3$.
The generated magnetic field should not influence the neighbouring superconducting qubits.
The magnetic shield should proved shielding from the local magnetic background field.

To achieve this goals, I started with simulating the solenoid and shield with the simulation software Comsol Multiphysics®.

4.2. Simulation geometry

The initial geometry was taken from an already existing simulation for a μ-metal shield for superconducting qubits. This was then adapted to the requirements outlined above.

During the design process, several options where evaluated, both for the dimensions of the coil and shields, as well as the number of shields.
Figure 4.1 shows the design installed in the cryostat for the first test.

The final simulated geometry consists of three concentric Cryophy cans with a wall thickness of 1 mm and closed bottom. A thicker wall thickness would have been desirable but the material stock options did not allow for this. The shields of the cans are spaced with a gap of 4 mm on all sides.
The inner working volume is 88 mm in diameter, and 256 mm in depth. For the top, a 1 mm Mu-Metal cap with a hole for the signal cables and mounting holes for the coil and sample is used.
The coil is represented as a cylinder with a length of 200 mm, a diameter of 73 mm and a wall thickness of 1 mm. Around all a air volume of 1 m radius and 1.5 m hight was also simulated to evaluate how the field extends out from the setup.

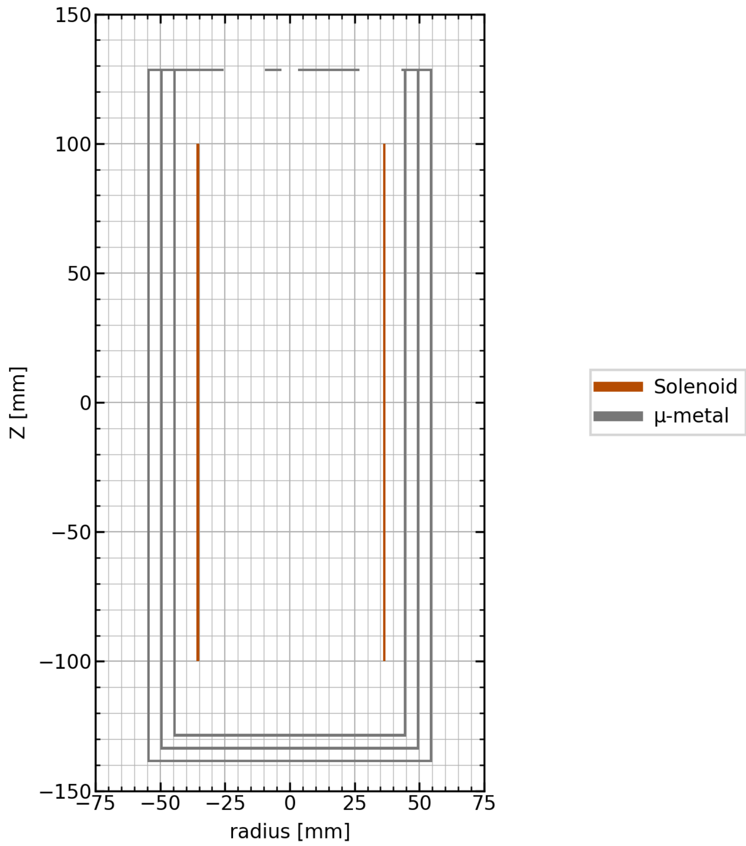

Figure 4.1.: Cross-section view of the simulation geometry with the Cryophy shields in gray and the solenoid in brown

4.3. Simulation results

For all following plots the field strength distribution along the z axis is taken for $r = 0$ and in radial direction for $z = 0$, in the coordinate frame of Figure 4.1, if not otherwise specified.

4.3.1. Background field shielding performance

In Figure 4.2 the shielding performance without any generated magnetic field is shown for one, two and three shielding cans and one top plate. For the cases of one and two shield cans, the inner most shields where removed in the modeling for the simulation. The background field is taken from Table A.1 and fixed at the surface of a cylinder of radius 0.5 m and hight of 1.5 m, centred around the shielding.

One shield reduces the magnetic background by two orders of magnitude and each additional shielding can by an other order of magnitude. For our targeted working range in the tens of mT we will have thereby a separation of the background field strength to

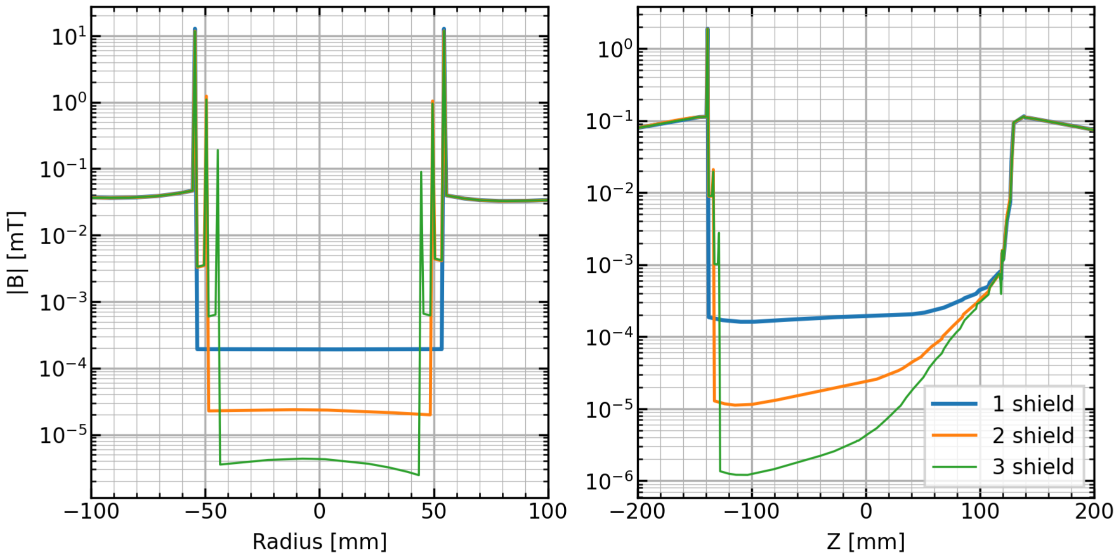

Figure 4.2.: Simulated shielding performance from external magnetic field with one, two and three shields in radial and axial direction.

working field strength of at least four orders of magnitude.

4.3.2. Shielding of internal generated field

The shielding of the internal generated field is the most important role of the cryophy shielding. Figure 4.3 shows the magnetic field with the same geometry as discussed for 4.2.

All three configurations perform very well in shielding the generated magnetic field by concentrating the field inside the cryophy. But we can also see for the given center field strength of 2.5 mT, that the field inside the cryophy already reaches approx. 300-400 mT. Considering the saturation field of approx. 800 mT, one shield is no longer sufficient for higher fields, therefore we opted to use 3 shields to stay on the save side.

4.3.3. coil constant determination from simulation

In Figure 4.4 I have plotted the simulation results for different currents. Despite the non-linearity of the permeability of Cryophy, as discussed in section 3.2, the field in the center of the solenoid scales linearly with the current. The coil constant is fitted to $(24.3449 \pm 0.0025)\,\frac{\mu\mathrm{T}}{\mathrm{mA}}$ and the inductance to $(0.456\,60 \pm 0.000\,05)\,\mathrm{H}$.

4.3.4. Homogeneity study of coil

As discussed in chapter 2, the geometry of the solenoid has a big influence on the magnetic field. The geometry of the surrounding magnetic materials also has a major

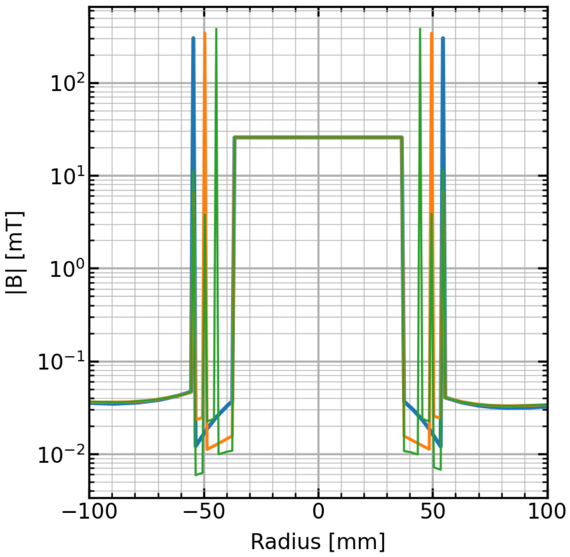

Figure 4.3.: Simulated shielding performance of the internal generated magnetic field with one, two and three shields in radial and axial direction.

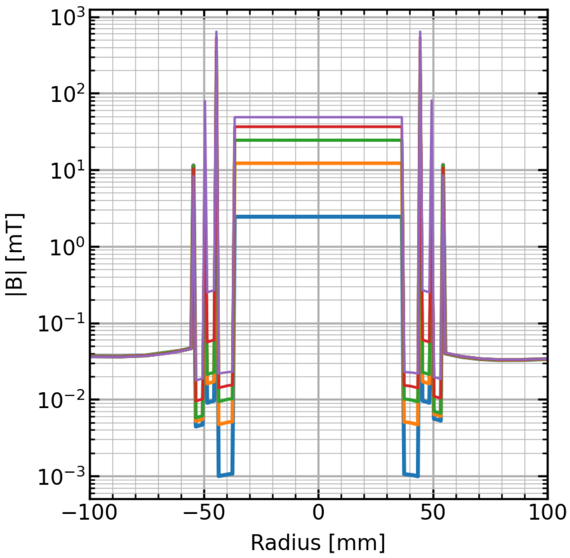

Figure 4.4.: Simulation of the absolute field strength generated by different solenoid currents.

influence on the magnetic field.
For the optimal current distribution in vacuum, a solenoid with the length of 20 cm needs double the current density for 18.6 mm on each end. The same coil inside the magnetic shield is shown in Figure 4.5 as the purple line. Since the shield acts as an amplifier for the magnetic field at the ends of the solenoid, we need less additional

current at the ends.
The placement of the solenoid with respect to the end plates of the inner shield is also very important. The variable b gives the distance between the bottom end of the solenoid and the bottom end of the inner shield in mm. For $b = 28$ mm, the solenoid is centered in z-direction between the top and bottom plates of the shield. For the two cases where $b = 10$ mm and the solenoid is therefore not centered (blue and orange curves in Figure 4.5), it is necessary to compensate with different amounts of additional windings on each end of the solenoid.
While a decent homogeneity in radial direction is possible with the asymmetric placement of the solenoid, it is necessary to have the solenoid centered with respect to the end plates do archive good homogeneity in axial direction too. The green curves show the best current distribution for a symmetrical placed solenoid for a step resolution of 1 mm, for the double current density regions into account. This resolution limitation was done due to the difficulty in winding the solenoid. This will be discussed later in more detail.
The red curves show the magnetic field strength for a symmetrically placed solenoid with asymmetric windings at the ends, as it is the case with the final fabricated solenoid and will be discussed in section 5.4 in more detail.

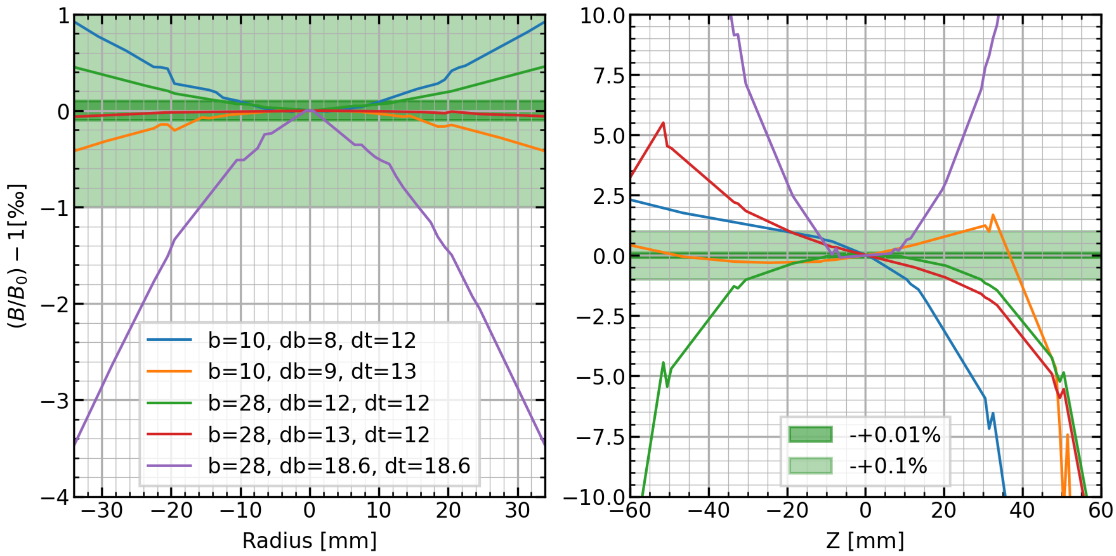

Figure 4.5.: Homogeneity of the center region in the solenoid, shown as deviation from $B(0,0)$ in radial and axial direction. b is the distance in mm between the end of the solenoid and the bottom of the inner most shield. For $b = 28$ mm, the solenoid is centered inside the inner most shield in z-direction. db and dt are the length in mm of the section with double the current density inside the solenoid.

Especially for the asymmetric cases shown in Figure 4.5, the simulation shows some non-continuous picks. This is due to bad mesh quality. I tried several different methods to generate the mesh for the simulation and the best result is shown here.

4.3.5. Modified shield design after first test

After the first test run, see section 6.4, we saw that the shield was not able to adequately suppress the magnetic field generated by the solenoid. In order to improve the shielding performance, we explored the possibility to replace the outer most cryophy can with a superconducting aluminium can.

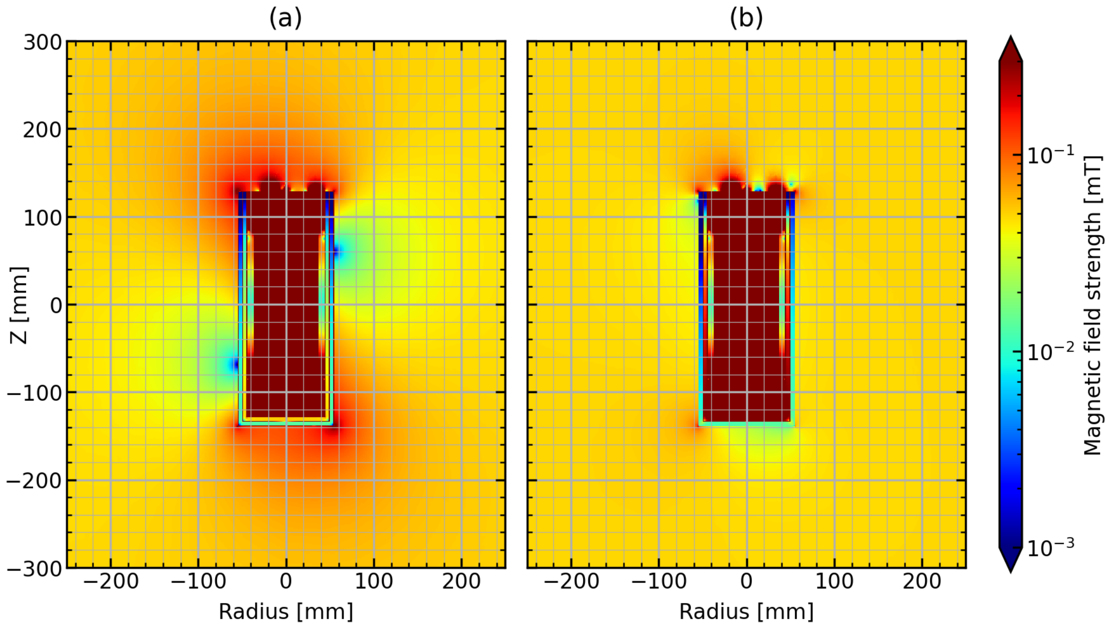

Figure 4.6.: Magnetic field strength colored between 0.001mT and 0.4mT. a) Magnetic shield setup with the shield design discussed in section 4.2. b) Same overall geometry as in a, but the outer most cryophy can has been replaced by a superconducting aluminium can.

Figure 4.6 shows a comparison between the original shield (a) and the new shield with the superconducting aluminium can (b). Aluminium is a type I superconductor below 1.17 K, with a critical field of approx. 10 mT. Below the critical field, a type I superconductor expels all magnetic field. With this combination of two cryophy cans and one outer superconducting aluminium can, the stray fields we see in Figure 4.6 (a) are greatly reduced.

4.4. Introduction to the Bluefors XLD400 dilution refrigerator

We are using the XLD400 dilution refrigerator from the company Bluefors. Figure 4.7 shows a view of the inside of the cryostat with the different temperature stages labeled.

The cryostat is suspended from the top. The upper most stage, not visible in the image, is the 50 K stage, followed by the 4 K stage, which are both cooled by pulse tubes. The still stage has a operating temperature of approx. 1 K and is cooled by pumping on a liquid ^{4}He bath. The cold plate has a operating temperature of approx. 0.1 K. The mixing chamber stage reaches operation temperatures down to 7 mK.

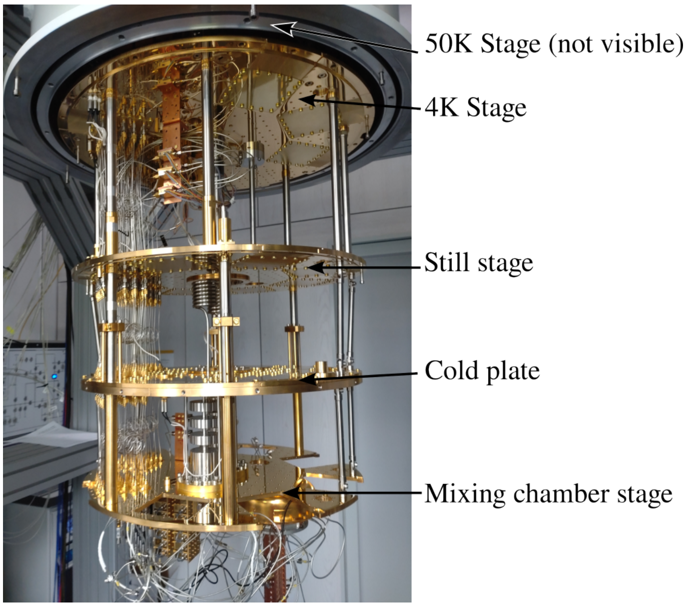

Figure 4.7.: Image of the inside the Bluefors XLD400 cryostat with the different cooling stages labeled.

4.5. Heat load estimations

4.5.1. Energy release in a quench event

The inductance of the improved solenoid is high compared to a Helmholtz coil with a similar coil constant. For the maximal expected current of 2 A, the energy stored in the improved solenoid equals 0.91 J. The release of this energy during a quench event will lead to a dramatic increase of the temperature of the stage the magnet is anchored to and could potentially damage the cryostat/dilution unit if attached to the mixing chamber stage. In order to protect the cryostat and the dilution unit, we have anchored the magnet to a higher temperature stage, in particular to the cold plate, which nominal operation temperature is approx. 100 mK.

4.5.2. Black body radiation of the solenoid body

Due to the temperature difference of the solenoid body compared to the shielding and sample assembly, we have to consider the black body radiation from the solenoid.

The solenoid body has a surface area A of approx. $0.1\,\mathrm{m}^2$ and will be anchored to the 100 mK stage of the cryostat.
With the Stefan-Bolzmann law

$$P = A\epsilon\sigma T^4 \tag{4.1}$$

for the energy P radiated from a black body with temperature T, the total energy radiated from the solenoid body can be estimated to 56.7 fW. The emissivity ϵ of copper is approx. 0.5, σ is the Stefan-Boltzmann constant and A the surface area.

The energy of the black body radiation is nearly three orders of magnitude lower than the cooling power of the cryostat at the mixing chamber stage, which for XLD400 is $16\mu W$ at 20 mK [2].

4.5.3. DC current leads between 4K stage and room temperature

Due to previous modifications done to our specific refrigerator, the factory high temperature superconducting current leads, indented for powering superconducting solenoids, could not be installed on time. Thus we opted to bundle 12 DC copper signal lines for each leg of the solenoid to achieve sufficient capacity to power the solenoid. This means that from the 4 K stage upwards, the current would lead to a heating due to the resistance of the copper wires.

According to the manufacturer of the cryostat, the maximal current capacity for a single copper wire is 1750 mA before damage was measured and without any current in the other wires. The safety limit is given as 75% resulting in 1300 mA. The resistance of the 35 AWG ($0.06\,\mathrm{mm}^2$) copper twisted wire pair is given as smaller than $2\,\Omega$.
An exact measurement across four twisted wire pairs, shorted at the 4 K stage, resulted in an average resistance of $(0.57 \pm 0.02)\,\mathrm{m}\Omega$ per single wire under cryogenic condition.
With this we can calculate the heat load onto the system at the safety limit with $P = I^2R$ to 0.96 W.
Since the heat load is the limiting factor for multi stranded cables, the maximal current for N wires connected in parallel, inside the same cable is $I_{total} = I_{single}\sqrt{N}$. For the 24 DC lines in one cable, this results into a total current at the safety limit of 6.37 A. Because the cable will carry both the current to and from the solenoid, the total current seen by the cable will be twice the current from the solenoid. Thus the maximal current that can be provided by a 24 DC line cable split in two 12 DC line parallel strands is 3.18 A.

4.6. Build process

4.6.1. CAD-model

Most of the actual designing of the parts was done in SOLIDWORKS®, with some designs development in Autodesk Inventor. With a 3D-model of the XLD400 dilution refrigerator provided by Bluefors, exact fit and placement of the different components was ensured. Figure 4.8 shows the refrigerators mixing chamber plate (lower) and cold plate (upper), with the final setup attached.

Figure 4.8.: 3D model of the final shield and solenoid assembly inside the Bluefors XLD400 cryostat. The upper copper colored plate is the cold plate, the lower copper colored plate is the mixing chamber plate. Also in copper color are the two plates for the mounting of the solenoid holding rods on the cold plate and the shield on the mixing chamber plate.

The solenoid is attached to the cold plate with three copper rods with a diameter of 14 mm and a thinned section of 10 mm where they pass through the magnetic shield.
The shielding assembly is attached to the mixing chamber plate via a copper interface plate, with throughputs for coil-holding rods and microwave cables as well as the hole for mounting the sample holder. All copper components are build from oxygen-free, high-conductivity copper (OFHC-copper).
The shielding cans have a flange on the top end with which they are mounted to the interface plate by 8×M4 bolts. The top shield is sandwiched between the interface plate and the inner most can.

4.6.2. Solenoid construction

The copper body of the solenoid was fabricated by the workshop subdivision of WMI from a 1.5 mm thick and 200 mm long cylinder with the inner diameter of 70 mm. At the upper end a 10 mm tall and 5 mm thick ring was added, providing space for mounting holes and additional stability. At the lower end a 5 mm tall and 5 mm thick ring was added for stability.

The superconducting solenoid is winded with a superconducting NbTi wire. The bare diameter of NbTi together with copper mantel is 0.079 mm in diameter and together with the isolation layer amounts to 0.101 mm in diameter. The copper to superconductor ration is 1.5 : 1.

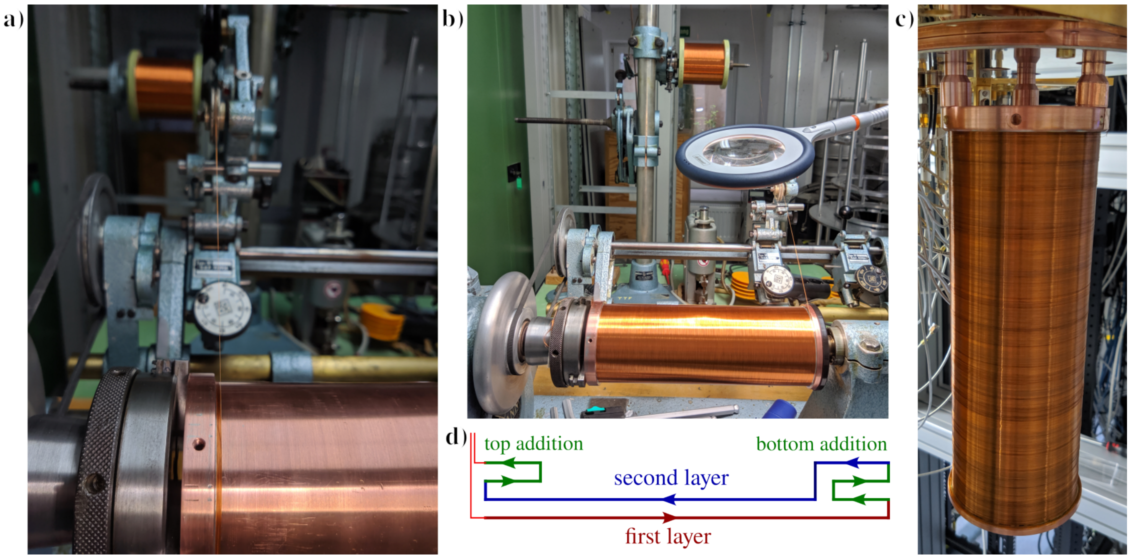

Figure 4.9.: Photos demonstrating the winding setup and process. a) Beginning of the winding process. b) First completed layer. c) Finished solenoid installed in the cryostat. d) Schematic view of the winding path during the winding process.

I have performed the coil windings following the pattern shown in Figure 4.9(d), starting at the top end, as depicted in Figure 4.9(a), and finishing at the same side after having two full and 4 partial layers, so that the wire ends can be twisted into a twisted pair. Figure 4.9(b) shows the solenoid after the first layer was completed and a layer of GE-varnish was added to bond it down. Figure 4.9(c) shows the finished solenoid installed inside the cryostat without the shielding cans.

In total, three solenoids have been winded. The first solenoid was done with normal copper wire with a total diameter of 0.11 mm, to test the winding procedure and the winding machine.

The second solenoid was done with superconducting wire. However, multiple shorts between the first layer and the copper body have been formed. To mitigate this problem in the second attempt, the body of the third solenoid was coated with GE-varnish prior winding the first layer.

During the winding of the lower section of the additional windings from the third solenoid, the number of windings was miscounted and 26 more windings have been added, as compared to the design. At this wire thickness this corresponds to a 1.3 mm longer addition layer. This leads to the shift of the optimal sample position, as well as a changed field distribution with decreased field homogeneity. The result of this change will be discussed in the next chapter.

5. Characterisation of solenoids at room temperature

In the design and modeling chapter, we looked at the axial and radial field distribution inside the coil. To verify the simulation, we measured the coils along the center line and compared the measurement to the simulation results. Due to the space restrictions inside the cryostat, the spacial field strength distribution inside the coil can not be measured inside the cryostat and has to be done at room temperature.

5.1. Measurement setup

The setup depicted in Figure 5.1, differs from the design for the cryostat, but the position of the solenoid within the shield, is the same. The solenoid together with the shielding is suspended by the same copper plate. This ensures, that the coil and shields are held in the same position as they will be in the cryostat later.

The axial field probe used in this setup, is the 'AS-UAP GEO-X' axial probe from Projekt Elektronik. The probe is attached by an aluminium bracket to a brass tube (see Figure 5.1 a), which is fed through the hole for the microwave cables in the μ-metal and copper plates (see Figure 5.1 b). On the top side, the probe is attached by an identical bracket to the spindle of the milling machine. The assembly is attached to the table of the milling machine and centered to the middle of the coil. The digital read-out of the milling machine is used to accurately position the probe along the center axis of the coil during the measurements.

During the field homogeneity measurement, the magnet has been power by a Keythley 2230G-30-1 DC power supply. We where not able to use the more precise CAEN FAST-PS 0520-100 used later to power the magnet in the superconducting state, since it was not able to handle the high resistance of the coil at room temperature and miss-regulated the current.

5.2. Axial field probe

Since at room temperature, the current is limited to only a few mA, the field probe needs to be sensitive in µT ranges. For this, we choose the 'AS-UAP GEO-X' axial probe from Projekt Elektronik. It has three sensitivity ranges with the maximal fields of 2 µT, 20 µT and 200 µT. The probe is comprised of a small coil with an internal diameter of 5 mm diameter and a length of 22 mm. For the axial measurements in the next sections,

Figure 5.1.: Setup for measurement of axial field distribution as mounted on an milling machine with digital read-out. a) View from the bottom at the field probe attached to the mounting rod. b) Side view of the solenoid without the three shielding cans. c) Completed measurement setup with shielding cans installed.

this geometry will result in an moving average along the axis and an smoothing of the field.

5.3. Copper test coil

As a practice and testing of the coil body design a copper test coil was first build and measured. This coil does not have the additional windings as discussed in the previous chapters. The simulation for the comparison has been changed accordingly to this.

The normal copper coil is 200 mm long, has 3389 windings of 0.1 mm copper wire.

The total resistance is $1.753\,\mathrm{k\Omega}$.

The coil constant is measured to be equal to $(20.78 \pm 0.21)\,\mathrm{mT/A}$ and the inductance to $(0.303 \pm 0.003)\,\mathrm{H}$. The theoretical estimated values are $21.29\,\mathrm{mT/A}$ and $0.277\,\mathrm{H}$.

Since the calculated values are for the ideal scenario in empty space, the measured and calculated values do not overlap within the error of the measurement, but are close enough to build trust in the measured results.

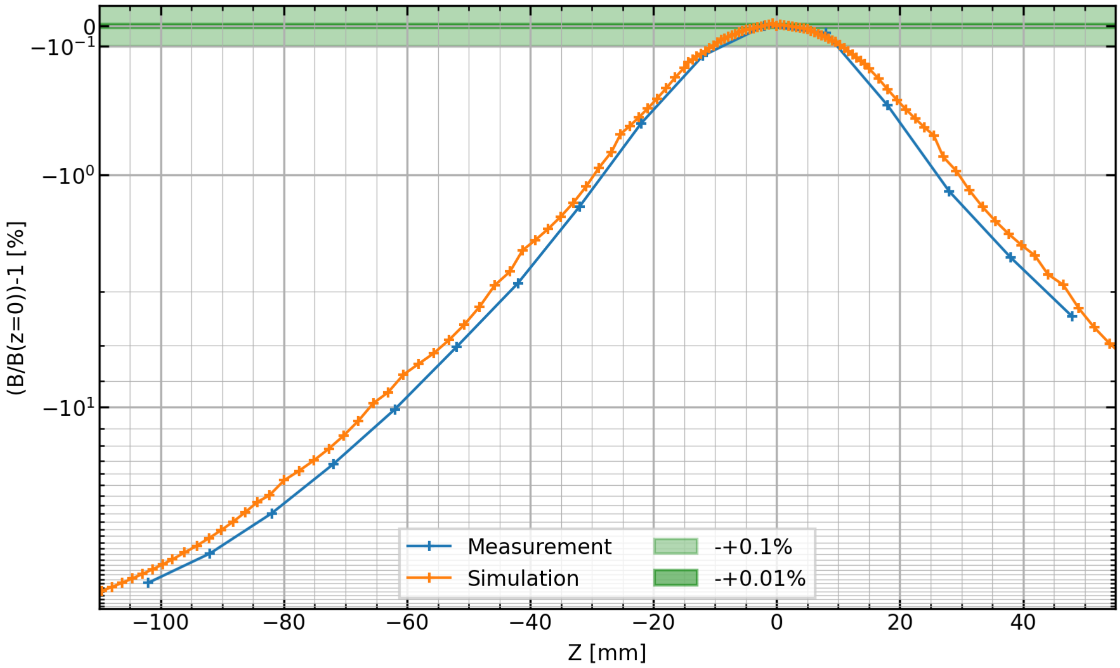

Figure 5.2.: Relative field strength along the center axis of the solenoid. The zero coordinate is set to the center of the solenoid.

Figure 5.2 shows the measured field strength, B, normalized to the field in the center, $B(z=0)$, of the solenoid in comparison to the simulation of the identical geometry. The measurement and simulation are in a very good agreement, and thus the simulation allows to predict the field strength inside the shielded solenoid with a high precision.

5.4. Superconducting coil

The superconducting solenoid discussed in this section is the third solenoid wound. The solenoid consists of 4360 windings in total. The first layer has 1944 windings, the addition on the bottom has 265 windings, the second layer has 1912 and the addition on the top has 239 windings.
The first and second layer stretch over the complete length of the solenoid as depicted

in Figure 4.9d).

5.4.1. Axial field distribution

Differences in the number of windings between these two layers will not effect the geometry of the field, as long as the density of the windings is homogeneous along the length of the solenoid.
The difference of 26 windings between the additional layers on the top and bottom does influence the field geometry greatly. As the result, the center of the field has shifted ca 40 mm downwards from the center of the solenoid.

I again measured the field distribution along the center axis of the solenoid, which is shown in Figure 5.3. The simulation take the difference in windings of the additions

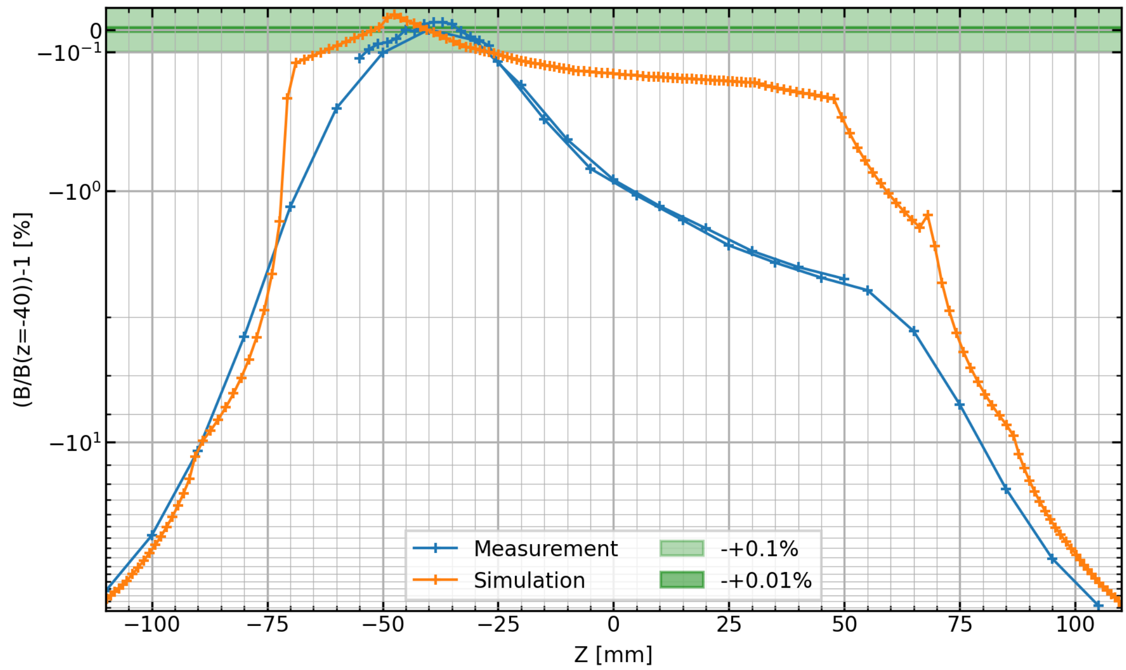

Figure 5.3.: Relative field strength along the center axis of the superconducting solenoid, the zero coordinate is set to the center of the solenoid.

into account. It predicts the shift of the maximum towards the bottom of the coil, but overall, the simulation is less reliable in predicting the field inside of the solenoid, as compared to the symmetric case of the copper coil.
At the ends of the solenoid, the simulation starts to agree with the measurements again. The sharp peaks of the simulation come from not fine enough mesh construction as discussed in chapter 4.

5.4.2. Coil constant measurement

As previously mentioned, the power supply we are using in the final setup was not able to drive the solenoids at room temperature due to the high resistance. This is especially notable in the measurement of the coil constant. Figure 5.4 shows the result for the Keithley power supply and the CAEN power supply. The both power supplies are set to constant current mode and should hold a set current. After switching on the power supply and setting the current to zero, both power supplies showed a drift in the voltage before reaching a steady state, while the current was still indicated as zero. This explains why for zero measurable current, we already see a minimal change in generated magnetic field. For this reason, the measurement of the CAEN power supply is in the further discussion ignored.

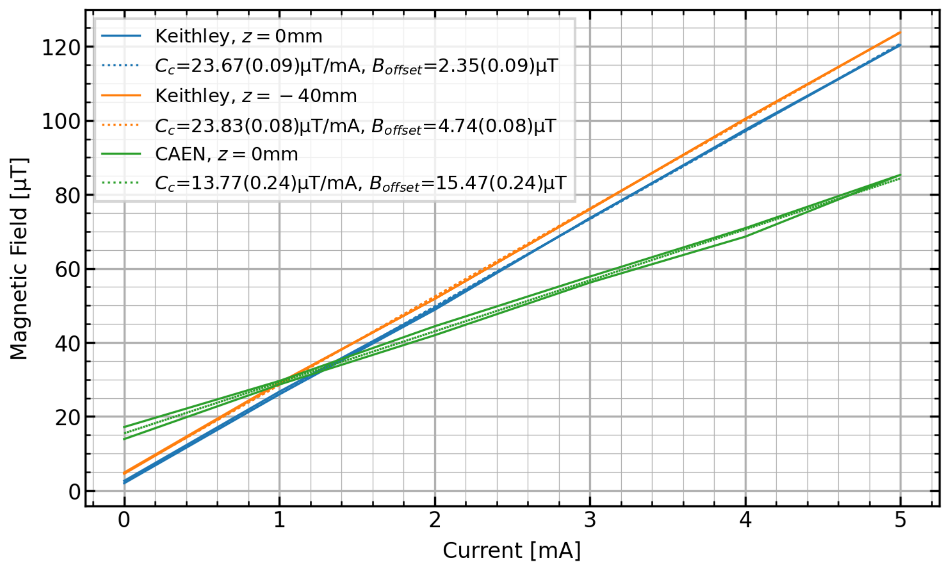

Figure 5.4.: Measurement of the coil constant with two power supplies and different positions along z.

	coil constant	inductance
sc-solenoid at $z = 0$	$(23.67 \pm 0.09)\ \frac{\mathrm{mT}}{\mathrm{A}}$	$(0.446 \pm 0.001)\ \mathrm{H}$
sc-solenoid at $z = -40$	$(23.83 \pm 0.08)\ \frac{\mathrm{mT}}{\mathrm{A}}$	$(0.447 \pm 0.001)\ \mathrm{H}$
simulation at $z = 0$	$(24.3449 \pm 0.0025)\ \frac{\mathrm{mT}}{\mathrm{A}}$	$(0.456\,60 \pm 0.000\,05)\ \mathrm{H}$
theoretical estimation	$27.30\ \frac{\mathrm{mT}}{\mathrm{A}}$	$0.460\ \mathrm{H}$

Table 5.1.

The results from the coil constant measurements are summarised in Table 5.1. As already discussed for the copper coil, we do not expect the values to agree completely due to the surrounding μ-metal. Additionally the solenoid has a different current density as the ideal coil, used for the derivation of the theoretical estimate. It has to be noted that the permeability of the shield is temperature and field dependent. Since we are only measuring very small fields and at room temperature, the coil constant has to be confirmed for cryogenic temperatures with additional measurements at cryogenic temperatures. One can also see that the coil constant is independent of the position inside the coil.

6. Characterisation of solenoids at cryogenic temperature

6.1. Measurement setup

The measurement setup shown in Figure 6.1 consists of a Keysight P5003A 14GHz vector network analyser (VNA), a CAENels FAST-PS 0520-100 power supply and a windows computer with Matlab for running the measurement scripts. The cryostat is a Bluefors XLD400.

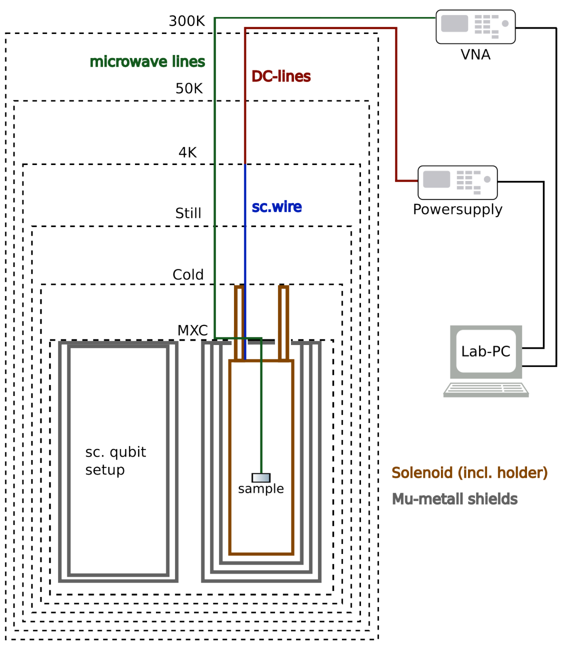

Figure 6.1.: Schematic overview of the cryostat and measurement system. On the left, the cryostat is schematically depicted and its internal temperature stages are outlined. On the right, connection of the external measurement devices is shown.

6.1.1. Electron spin resonances spectroscopy

We are using electron spin resonance, short ESR, spectroscopy to measure the Zeeman effect of hyperfine levels in rare earth ions. With the ESR spectroscopy we measure the absorption by the rare earth ions of the transmitted microwave signal. [14]

The sample is glued on top of a superconducting transmission line which is patterned on top of a Si chip.

For rare earth ions like erbium, the ground states at very low temperatures can be described by the reduced Hamiltonian

$$H = \mu_B B \cdot g \cdot S + I \cdot A \cdot S \tag{6.1}$$

where the first term is the Zeeman splitting, with μ_B as the permeability of the material, g the g-factor and S the electron-spin operator. The second term is the hyperfine splitting, with the nuclear-spin operator I and hyperfine operator A.[4] The quadrupole term and nuclear Zeeman-effect have been neglected.

Applying a magnetic field lifts the degenerate state of the electron spin-1/2 system and transitions between the Zeeman splitting energy levels can be seen at very low temperatures when applying a microwave signal corresponding to the resonance condition

$$\omega_0 = \frac{e}{2m} \cdot g_B \cdot B_0 \tag{6.2}$$

with the microwave frequency ω_0, external magnetic field B_0, electron charge e, electron mass m.

6.1.2. Reference material for solenoid characterisation

Initially, we inteded to use DPPH (2,2-diphenyl-1-picrylhydrazyl) as a magnetic field reference due to its well known g-factor. However, we could not detect any signal from the DPPH sample, which was glued next to the ^{167}Er sample on the transmission line. This might be due to a bad positioning of the sample on the transmission line, leading to a small interacting volume, or due to an insufficient polarisation of the sample by the magnetic field. Nevertheless, we could detect a signal from the main ^{167}Er:7LiYF4 sample. This sample was already measured in a Fallen Duke cryostat with a superconducting solenoid magnet sitting below the sample position. This measurement can be further used as a reference for evaluating the field homogeneity and will be labeled as reference. The measurements inside the Bluefors XLD cryostat will be further label "XLD1", which is the internal designation used.

Ana Strinic also simulated the transmission spectrum of ^{167}Er doped into LiYF4 [11].

6.1.3. Signal processing

In the used setup, the VNA measures the transmission through the transmission line (S21 parameter). Since the sample signal was small and the background showed a strong magnetic field dependence, an adequat background removal was necessary to identify the sample signal. Figure 6.2 shows the data at different background removal steps.

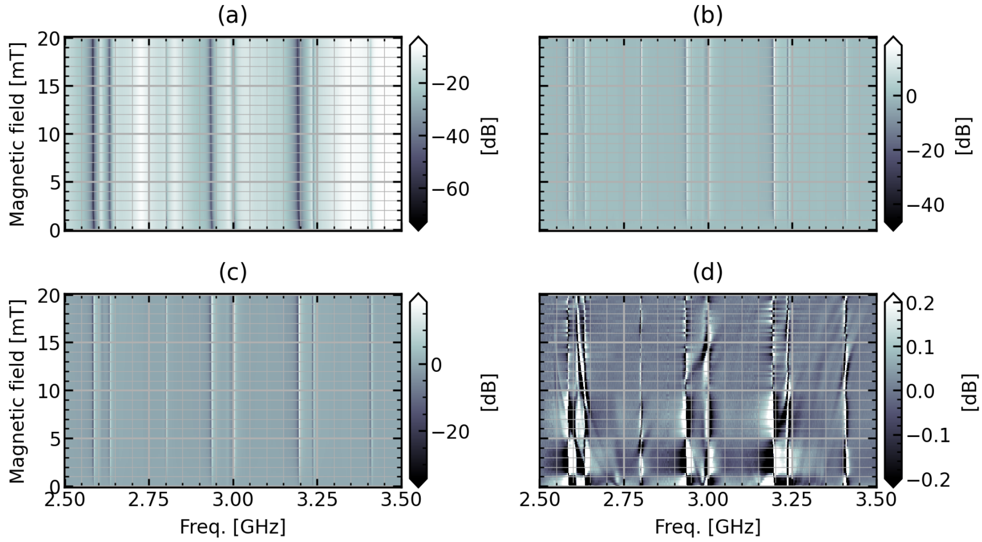

Figure 6.2.: Magnetic field sweep from 0 to 20 mT from 2.4 to 3.5 GHz. (a): raw S_{21} signal as captured from the VNA. (b): S_{21} minus the background measured before the sweep. (c): Fitted background map from (b) by using local regression. (d): final signal with background and fitted background map removed.

This background can mostly be removed by measuring a reference background at zero magnetic field before a measurement and subtracting it from the measurement as shown in Figure 6.2(b). Additionally, the background also changes with the magnetic field for each frequency differently. To compensate for this, the best working method I found is to fit a polynomial regression of 3^{rd} degree for each frequency over the whole range of the data-set. A 3^{rd} degree polynomial was found to be the highest polynomial to replicate the background, without altering the shape o the absorption lines seen in the spectra. The result of this fit is shown in Figure 6.2(c), and the final signal with both backgrounds removed is shown in Figure 6.2(d).
While this method is not perfect, especially for the broad frequency spans that include regions where the background is very strongly magnetic field dependent, as for example at 3 GHz, the method works good for smaller frequency ranges.
The data-processing method as described above is used to process all further discussed measured data, if not otherwise specified.

6.2. Determination of magnetic field homogeneity

The magnetic field homogeneity can be determined from the width of the absorption line of electronic spins. Expanding Equation 6.2 for a inhomogeneity term dB, we can see that the resonance absorption frequency ω_0 gets broadened by

$$d\omega = \frac{e}{2m} \cdot g_B \cdot dB. \tag{6.3}$$

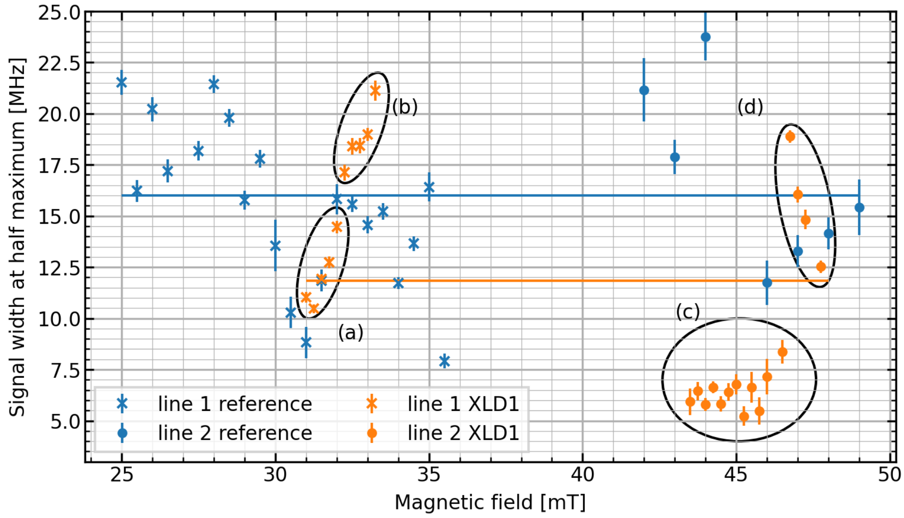

Figure 6.3.: Width at half maximum of two absorption lines at different field strength from the reference measurement in the Fallen Duke cryostat in blue and measurements performed within this thesis in orange. Areas (a)-(d) represent different fit quality, as shown in Figure 6.4.

This broadening of the absorption lines can then be compared to the measurement of the same sample in a different solenoid and thus the relative homogeneity of both solenoids can be compared. The profile of the absorption line is fitted with the Gaussian function.

Figure 6.3 shows the width at half maximum of two fitted absorption lines at different magnetic fields. The reference measurements of the Fallen Duke cryostat (FD) are shown in blue. The data marked with crosses in Figure 6.3 is from a absorption line in the frequency range from 3.43 GHz at 31 mT to 3.53 GHz at 33.5 GHz and the data marked dots from a different absorption from 3.43 GHz at 43.5 mT to 3.53 GHz at 48 mT.

One can clearly see that the FD data are more evenly grouped considering the errorbars, while the data from the new solenoid setup are spread out more, which is due to the strong background changes which decrease the quality of the fit.

To properly fit an absorption line, the spectra surrounding the absorption line hast to be flat. Figure 6.4 shows representative fits for each of the groups in Figure 6.3. Since there is insufficient flat data on either side of the absorption dip to properly fit to, none of these fits are optimal. The fits shown in Figure 6.4 (a) and (c), have the best fit quality, while the fit shown in Figure 6.4(b), has no sufficient flat data on either side of the absorption dip and is already near a strong field dependent distortion in the background. Figure 6.4(d) has some relatively flat data to the left, but the signal is very close to a strong background distortion, which influences the form of the absorption.

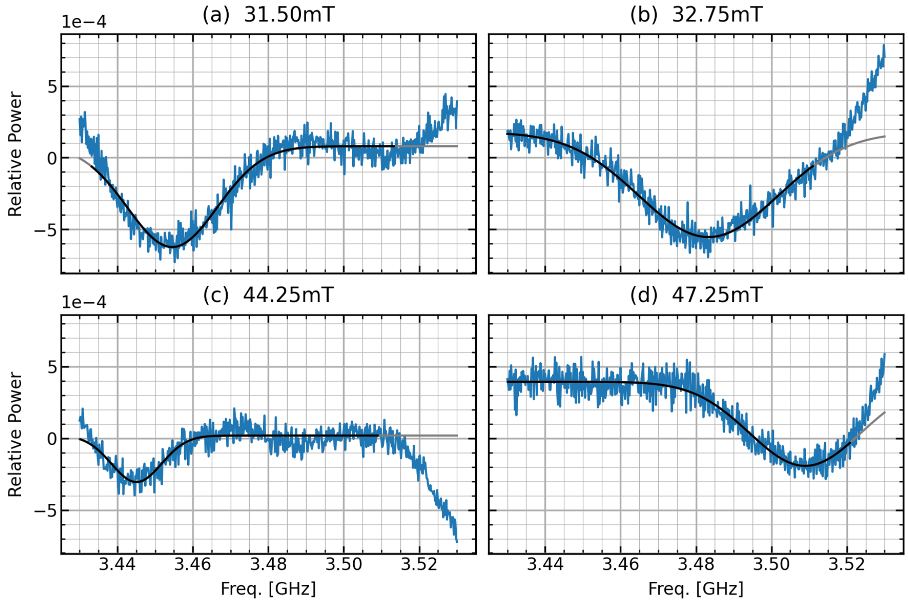

Figure 6.4.: This are the processed data and the respective fits, representing different groups in Figure 6.3. The Black line is the fit and extends over the frequency range that was used to fit and the gray line is the fit extended over the hole frequency range.

While the gathered data indicates that the solenoid has better homogeneity than the reference magnet in the Fallen Duke cryostat, the quality of the data is not good enough to give a conclusive answer over the actual performance of the solenoid.

6.3. Evaluation of coil constant and hysteresis of solenoid

As discussed in section 2.3, we expect hysteresis in the magnetic field, generated by the superconducting solenoid, to occur due to flux trapping.

Due to the strong field dependent background, measurement of one absorption line over a big magnetic field span proved challenging. In Figure 6.5, I plot the absorption line shown in Figure 6.6 for a field sweep from 5 mT to −5 mT and from −5 mT to 5 mT, together with the reference data and the simulated data. One can clearly see the hysteresis in the measured data from the magnetic field. Also the field-frequency dependence for negative and positive applied field is not symmetric, meaning that the field sensed by the sample is not linearly related to the applied current from which the Magnetic field is calculated.

The sensed field can be estimated by using the frequency position of the absorption

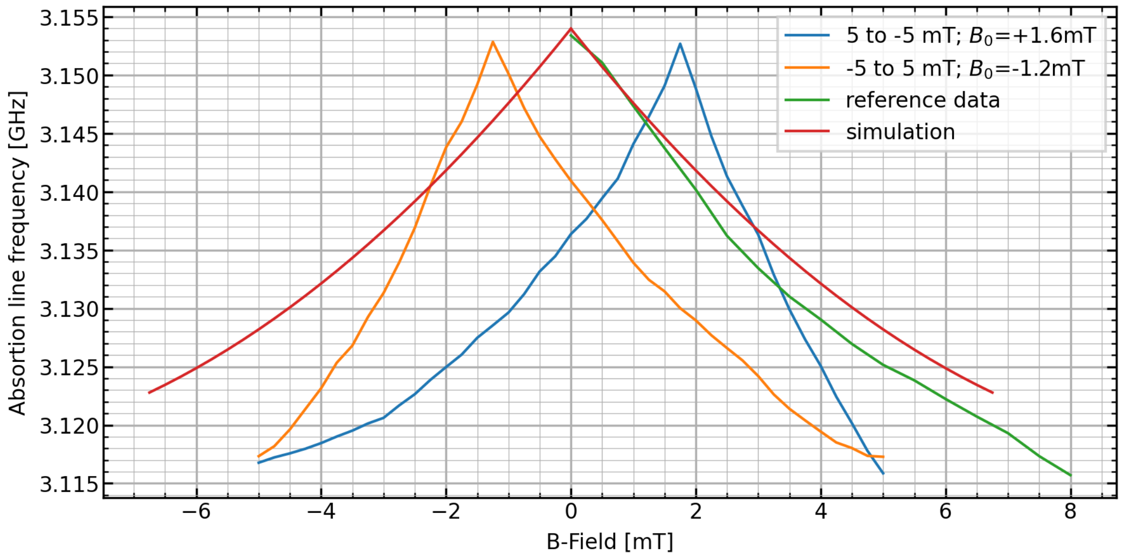

Figure 6.5.: Tracing of different absorption lines, the blue and orange lines are measured inside of this solenoid, in different applied field sweep directions. In green is the absorption line from the reference data and in red is the simulation data.

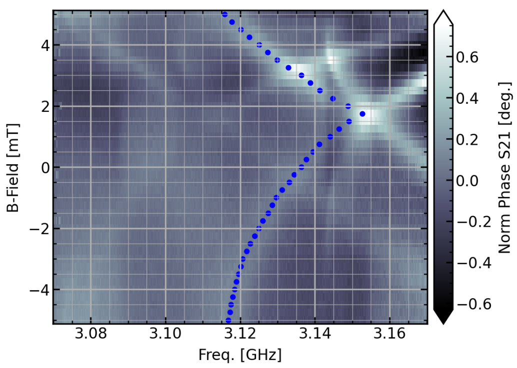

Figure 6.6.: Measured spectra with partially applied background subtraction procedure. Here the phase of the S_{21} signal is shown. Only the reference background was subtracted. The absorption line marked with blue dots, is the analyzed absorption line in Figure 6.5 in blue.

maximum for a given applied magnetic field and using the absorption line from the reference data to cross-reference the field sensed by the sample. Looking at the hysteresis loop shown in Figure 6.7 (a), we see that with the field sweep between $\pm 5\,\mathrm{mT}$ we do not reach the saturation region of the hysteresis. In Figure 6.7 (b), the field error is plotted against the applied field, as calculated from the current. After crossing the zero field, the field error saturates and then reduces again. From the field range shown here, we can not conclude, how the field error will change at higher fields.

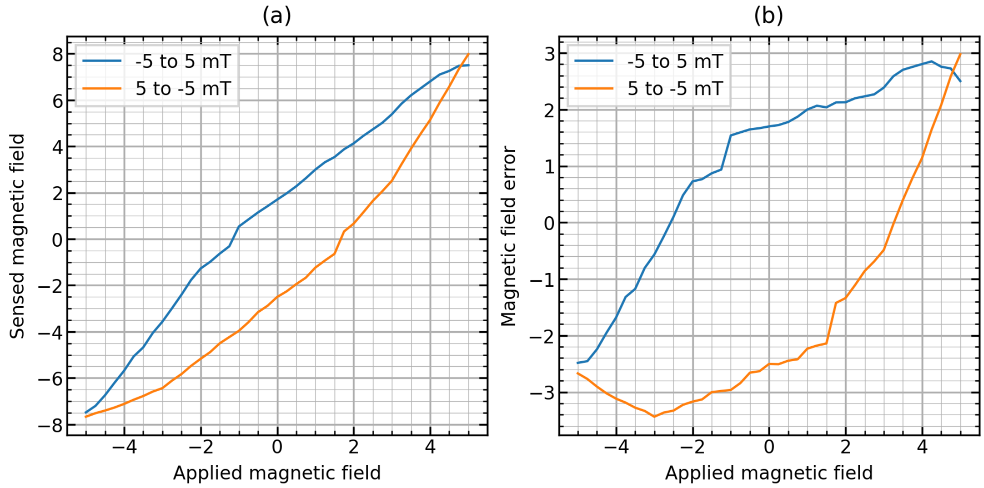

Figure 6.7.: Left: sensed magnetic field versus applied magnetic field for two field sweep directions, building an hysteresis loop. Right: Magnetic field error calculated as the difference between the applied field and sensed field.

To get a better hysteresis measurement in a bigger applied magnetic field range, I measured the spectrum between 3.65 GHz and 2.77 GHz for applied magnetic field ranges between ± 7.5 mT, ± 10 mT, ± 15 mT and ± 20 mT. For ± 15 mT and ± 20 mT, the spectrum was only captured in the field range of ± 10 mT, since the absorption lines are no longer with in the captured frequency spectrum outside of this field range. Shown in Figure 6.8 (a)-(d) is the result for these magnetic field sweeps from negative to positive fields. Due to a possible misalignment of the sample axis to the magnetic field direction at the sample position, we observe two absorption lines instead of one as expected and I can not compare it to the reference measurement.

The misalignment of the field direction and sample axis comes most likely from distortions of the magnetic field from trapped flux in the superconducting waveguide.

The offset of the zero field crossing is in all four measurements equal at approx. -1.4 mT. This shows, that for applied magnetic fields higher than ± 7.5 mT the offset no longer changes and thus, the saturation of the hysteresis is reached.

At higher applied magnetic fields, the data from Figure 6.9 shows a good alignment of the measured absorption frequency with the reference and simulation data with only a small offset of (0.75 ± 0.25) mT. The constant slope also indicates, that we are at this magnetic field strength in the saturated region of the hysteresis and the generated field is linear with the applied current.

With this we can limit a relative error in the coil constant at higher fields to approx. $2 \pm 1\%$.

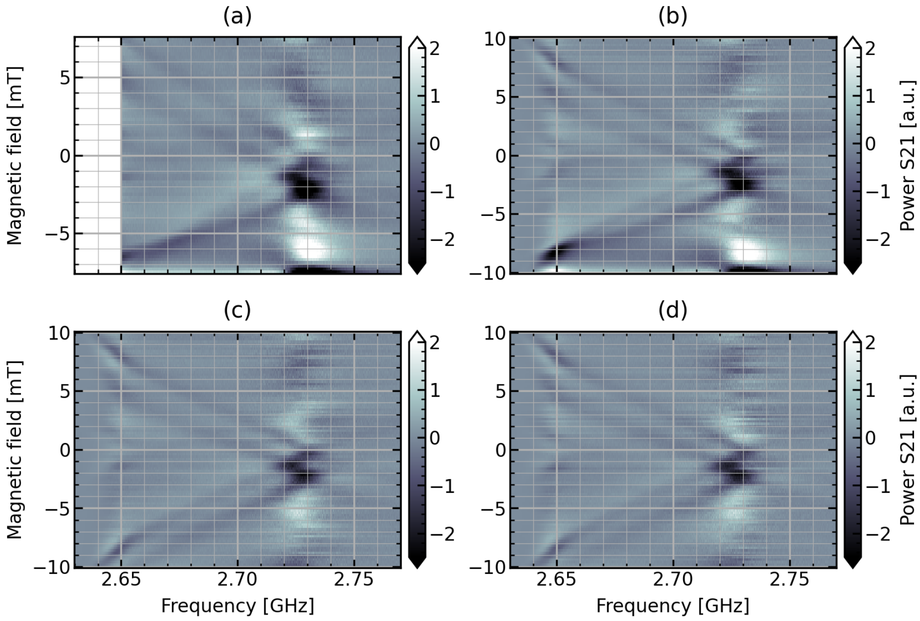

Figure 6.8.: Measured spectra for different applied maximal field strength prior the measurement. (a) $-7.5\,\mathrm{mT}$, (b) $-10\,\mathrm{mT}$, (c) $-15\,\mathrm{mT}$ and (d) $-20\,\mathrm{mT}$

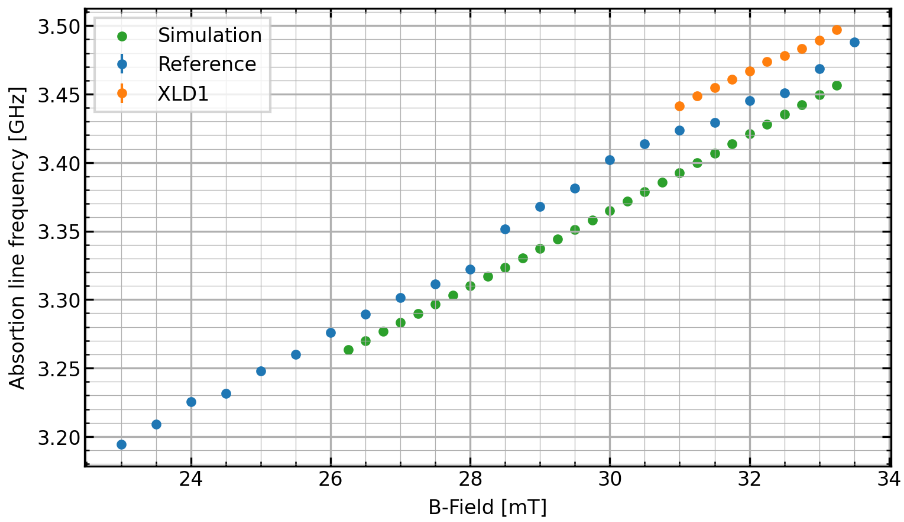

Figure 6.9.: Change of Absorption frequency for one Zeeman splitting transition, measured at higher fields.

6.4. Shield performance investigation

At Room temperature, the magnetic background field within the shields was measured to be $(0.052 \pm 0.006)\,\mu\mathrm{T}$, which corresponds to a reduction of three orders of magnitude compared to the local magnetic background field of 48.7 µT (section A.1).

To measure the shielding of the internal generated magnetic field from the solenoid, I did a joint measurement with Gerhard Huber from the quantum computing and information processing group at WMI, inside of the same cryostat (XLD1), to measure the influence of the magnetic field of the solenoid on a superconducting qubit. While changing the current of the solenoid over several hours, he continuously measured the frequency and T_2^* time from his superconducting qubit. The result is shown in Figure 6.10. The T_2^* time does not correlate with the applied current. The qubit frequency closely correlates with the applied current and indicates a strong dependence on the field. The continuous downwards trend of the frequency can be attributed to the slow change of the mixing chamber temperature. Since the direction of the change of the qubit frequency is coupled to the polarity of the solenoid current, we can attribute its change to the field and not to any temperature effects, which would be independent of the polarity. Gerhard Huber calculated for the frequency shift at 50 mT (2.11 A), a effective magnetic field, threading the squid loop and sample, of 0.47 nT.
Together with the two μ-metal shields of the qubit, a maximal total attenuation of 8 orders of magnitude, over a distance of approx. 25 cm, was archived.
Since the plane of the squid loop is not aligned with the magnetic field, the actual attenuation is expected to be slightly lower.

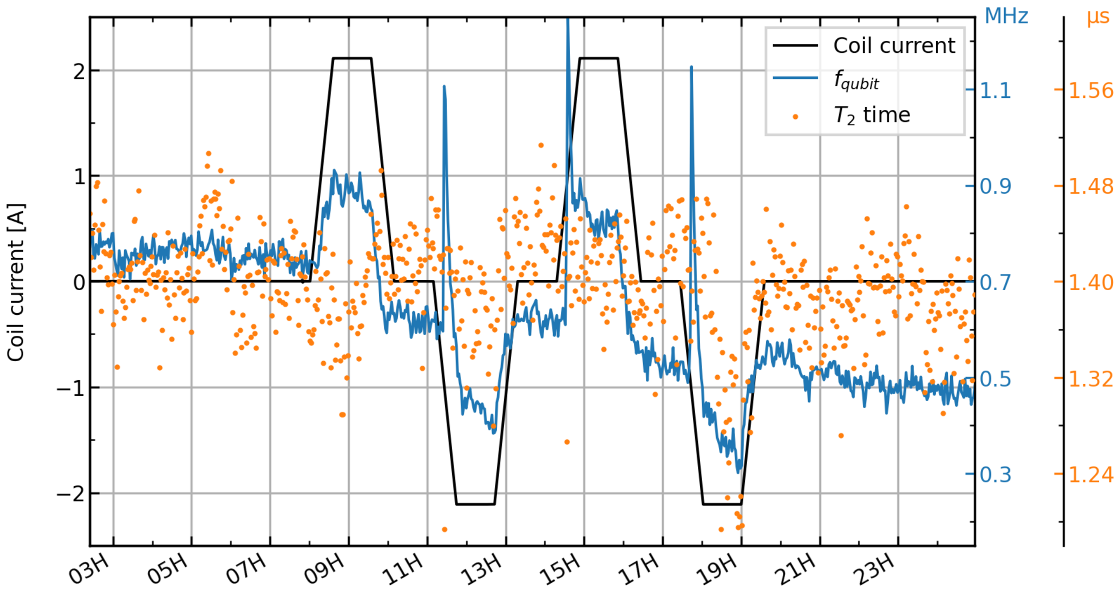

Figure 6.10.: Frequency and T_2^* time from the neighbouring superconducting qubit during current ramps of the solenoid.

We also observe three spikes in the frequency after the polarity of the solenoid current changes and crosses a threshold of approx. 1.1 A. At the same time we see a very short increase of the measured temperature at the mixing chamber stage in the order of >1.4 mK.

6.5. Thermal influence from the solenoid current on the cryostat temperatures

The cryostat continuously monitors the temperature of the 50 K, 4 K, still and mixing chamber stages. Figure 6.11 shows how the temperatures of the mixing chamber, still and 4 K stage change during solenoid current sweeps. The changes in temperature of the 50 K stage, coursed by the solenoid current, is negligible compared to the change over the course of the day and is not shown.

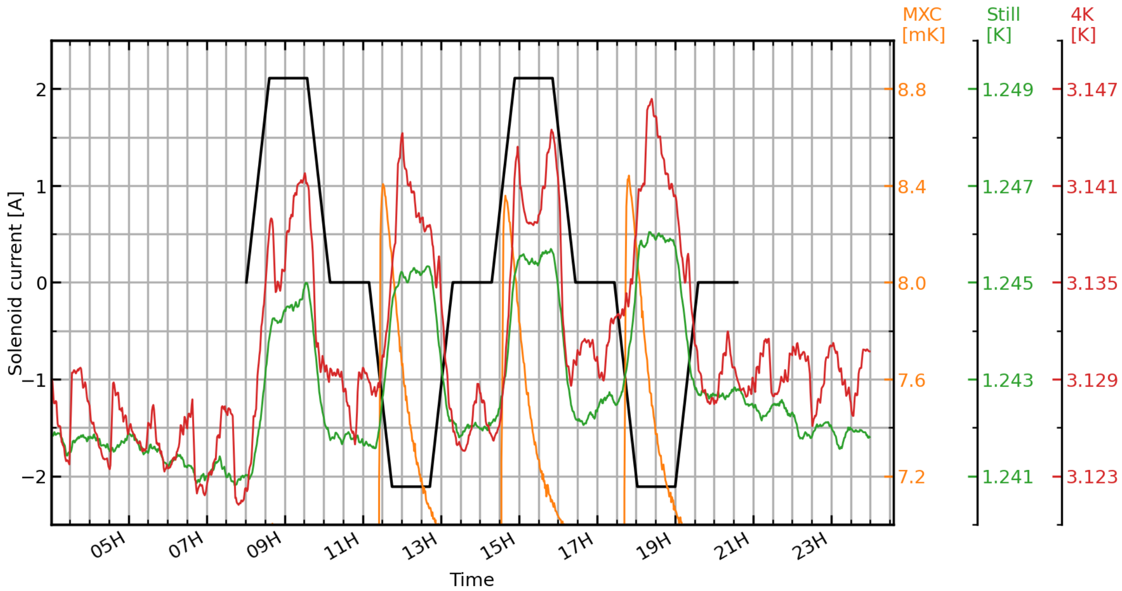

Figure 6.11.: Temperatures from the mixing chamber, still and 4 K stage during current ramps of the solenoid.

The superconducting wires from the solenoid are connected to the built-in copper DC lines at 4 K stage. Thus we expect the temperature dependence we see in Figure 6.11 from the 4 K stage. The still stage, which is beneath the 4 K stage, follows generally the temperature change of the 4 K stage. A temperature increase at the Still stage leads to a higher cooling power of the dilution refrigerator at the mixing chamber stage, due to a higher boil of rate of the ^3He, which is why we do not see any changes of the mixing chamber temperature directly correlated to the current.
The sensor of the mixing chamber is only calibrated down to 7 mK. The temperature spikes happen after a polarity change and at crossing values of ±1.1 A by the current. We relate this to the magnetization reversal accompanied by the release of magnetic energy in the form of heat when the field is strong enough. The energy release by this

event is estimated to be 0.4 mJ. We also saw no change in temperature when switching polarity below 1 A solenoid current.

7. Summary and outlook

In this thesis I showed the potential of an improved solenoid design for providing a highly homogeneous magnetic field in an very small footprint. I compared it with commonly used coil designs like the Helmholtz coil and a plain long solenoid mathematically and with simulations in the presence of a magnetic shield.
Based on the simulations, I constructed a prototype solenoid which we tested in an cryogenic environment.
Due to to a highly magnetic field dependent background, the extraction of useful data for characterising proved challenging and a full characterisation was not possible in the limited time frame of this thesis.

For two absorption lines, the width of the absorption has been fitted and compared to the reference data. The result of this indicates an similar if not better homogeneity of the field at the sample position.

At higher fields, the effects of the hysteresis diminished and the coil constant, measured at room temperature, holds up for higher fields with in a two percent window.

The shielding performed very well at shielding the interior from the local magnetic background at room temperature by reducing the field strength by an order of three magnitudes. At millikelvin temperatures, the shield was not able to fully suppress the generated magnetic shield towards the neighbouring superconducting qubits.

For better suppressing of the generated magnetic field we are in the process of replacing the outer most cryophy can with a superconducting aluminium can, which in simulations, promises better confinement of the generated magnetic field.

Since we suspect that the superconducting waveguide which was orientated perpendicular to the magnetic field, trapped flux and added to the hysteresis, we will change its orientation to be parallel to the magnetic field to reduce trapped flux. Additionally we will add a fresh DPPH sample, in order to try measuring it during the next cool down circle.

A. Appendix

A.1. Local background field

Table A.1 shows the background field in North, East and Up direction at the location of the WMI building, according to [9]. This is used as input for the simulation to simulate the shielding performance with two or three shields. The results can be seen in 4.2.

Direction	B-Field	H-Field (Vacuum)
+x(North)	20.9696 µT	16.6876 $\frac{A}{m}$
+y(East)	1.4878 µT	1.1840 $\frac{A}{m}$
+z(Up)	43.9493 µT	34.9748 $\frac{A}{m}$
Total	48.7183 µT	38.7699 $\frac{A}{m}$

Table A.1.: Earth background Fields [9]

A.2. Technical drawings

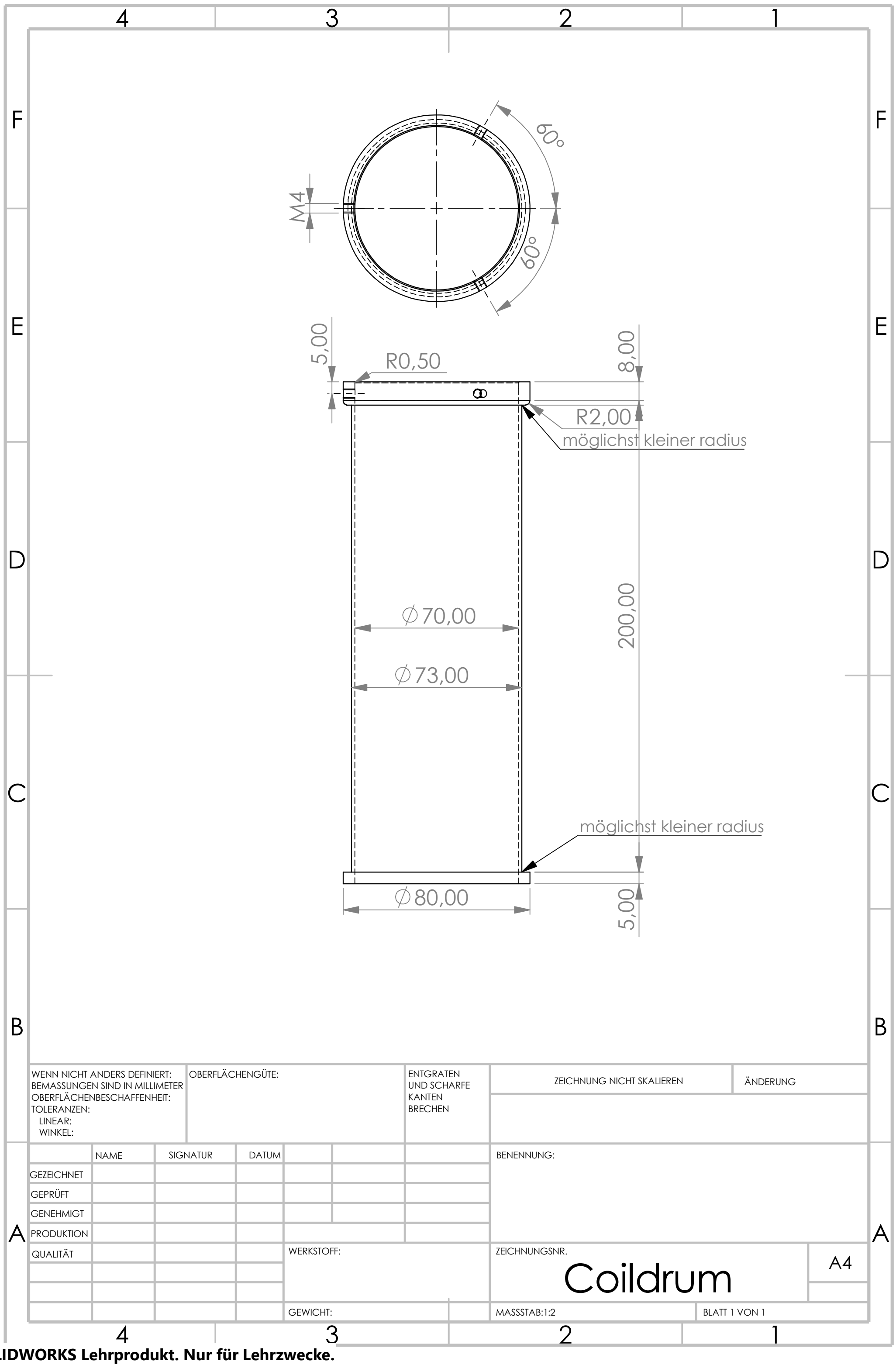

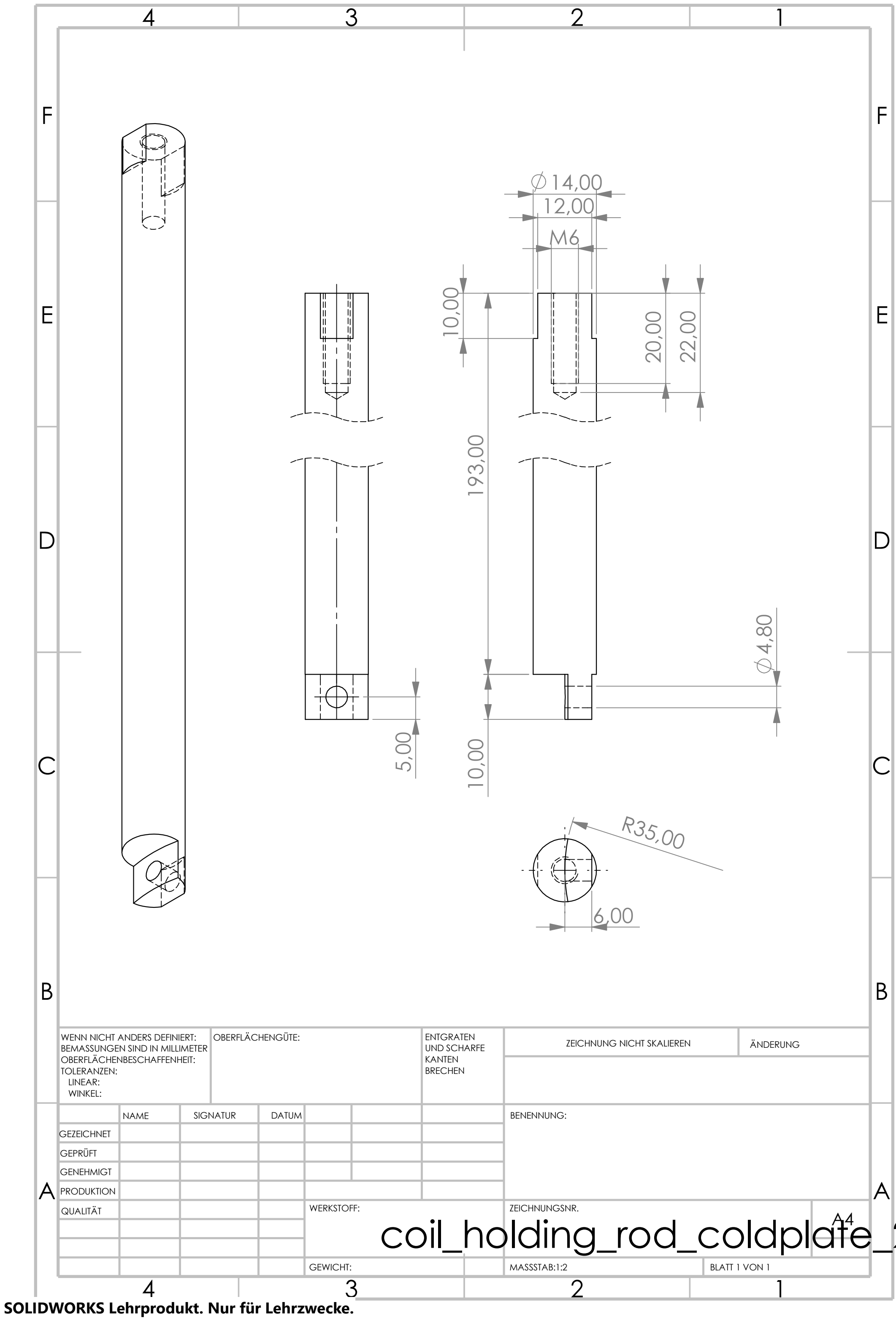

4
3
2
1
F
E
D
C
B
A
∅14,00
12,00
M6
10,00
20,00
22,00
193,00
∅4,80
5,00
10,00
R35,00
6,00
WENN NICHT ANDERS DEFINIERT:
BEMASSUNGEN SIND IN MILLIMETER
OBERFLÄCHENBESCHAFFENHEIT:
TOLERANZEN:
LINEAR:
WINKEL:
OBERFLÄCHENGÜTE:
ENTGRATEN UND SCHARFE KANTEN BRECHEN
ZEICHNUNG NICHT SKALIEREN
ÄNDERUNG
NAME
SIGNATUR
DATUM
BENENNUNG:
GEZEICHNET
GEPRÜFT
GENEHMIGT
PRODUKTION
QUALITÄT
WERKSTOFF:
ZEICHNUNGSNR.
A4
coil_holding_rod_coldplate_2
GEWICHT:
MASSSTAB:1:2
BLATT 1 VON 1
SOLIDWORKS Lehrprodukt. Nur für Lehrzwecke.

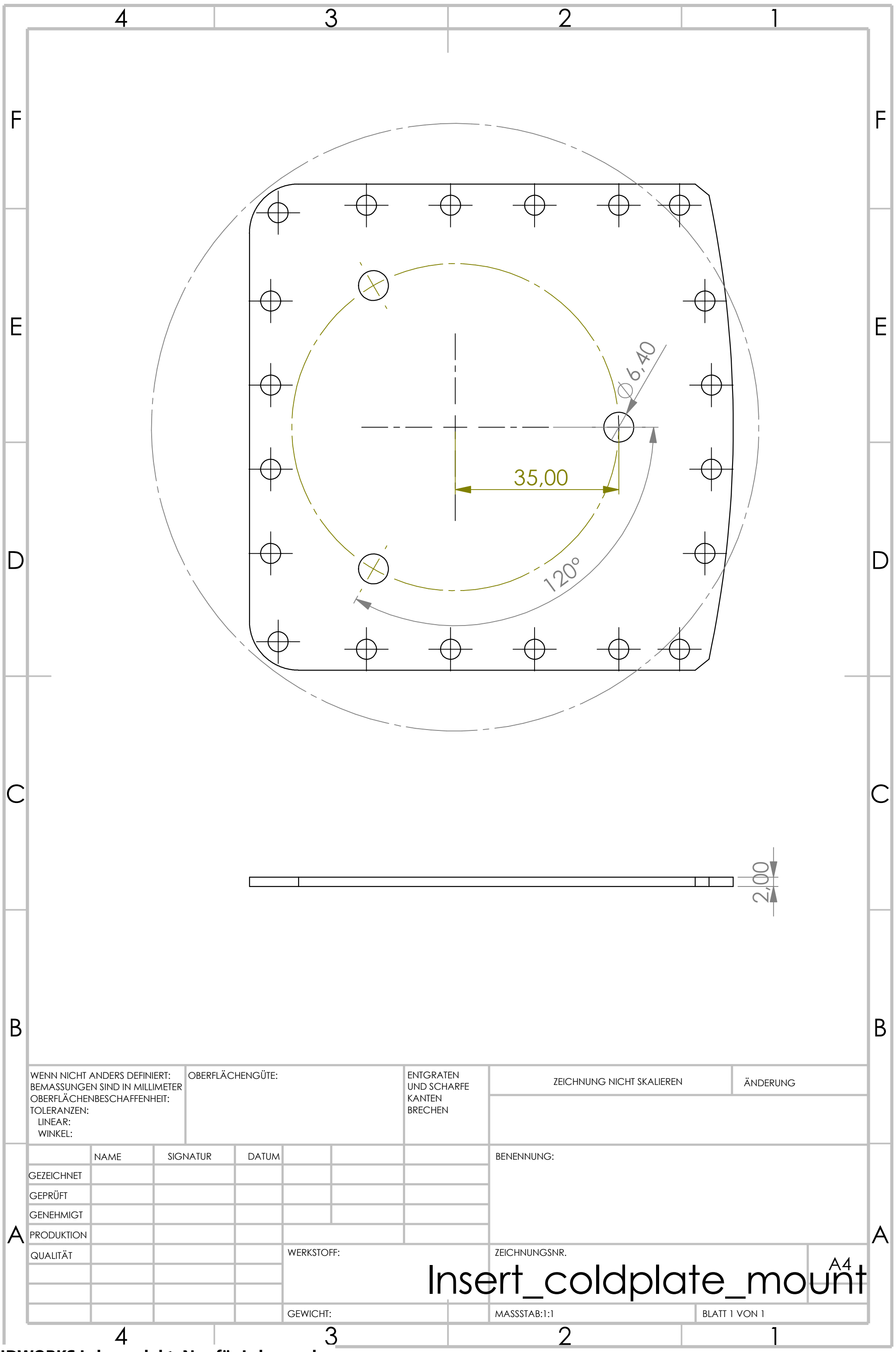

SOLIDWORKS Lehrprodukt. Nur für Lehrzwecke.

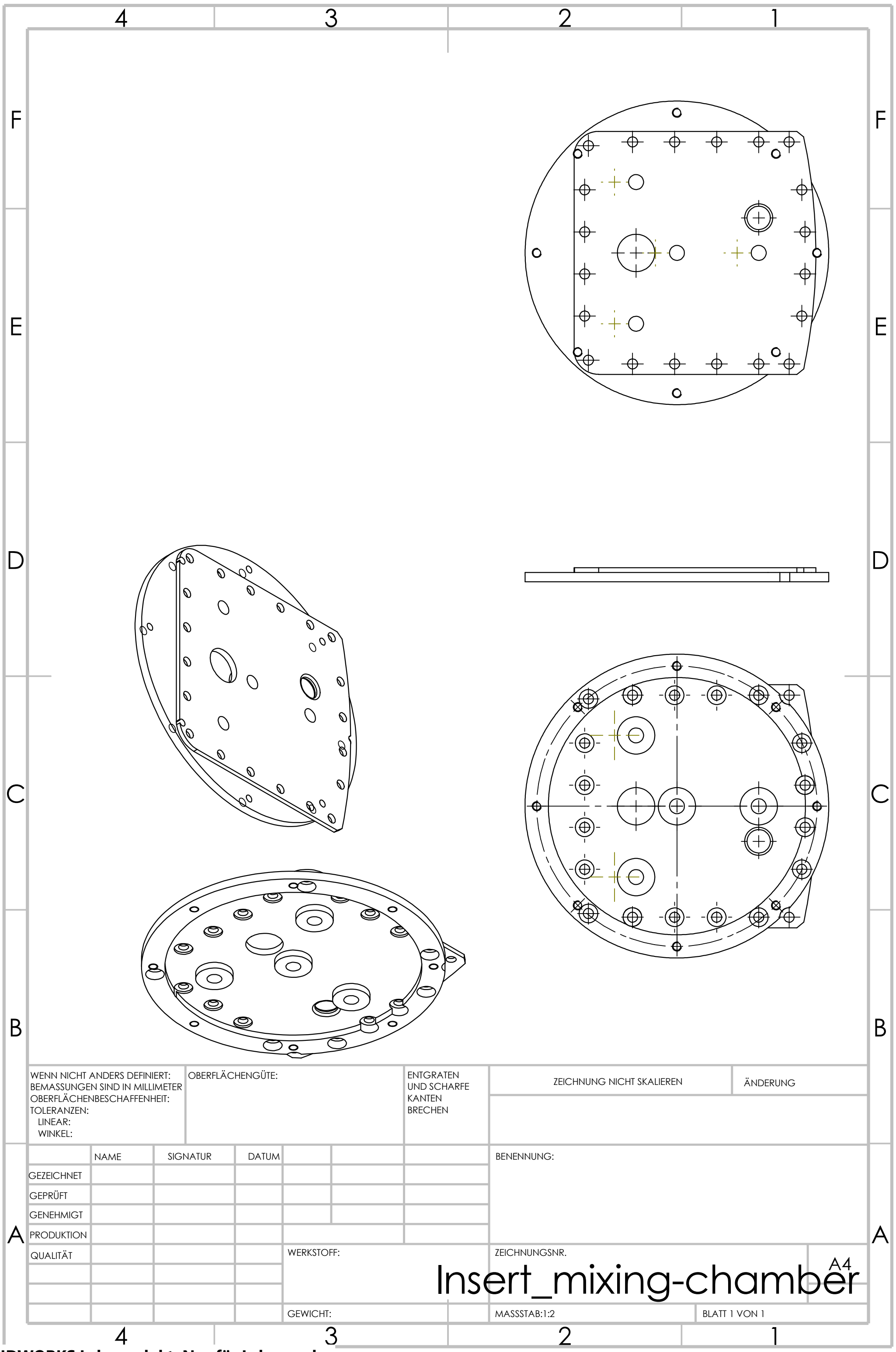

SOLIDWORKS Lehrprodukt. Nur für Lehrzwecke.

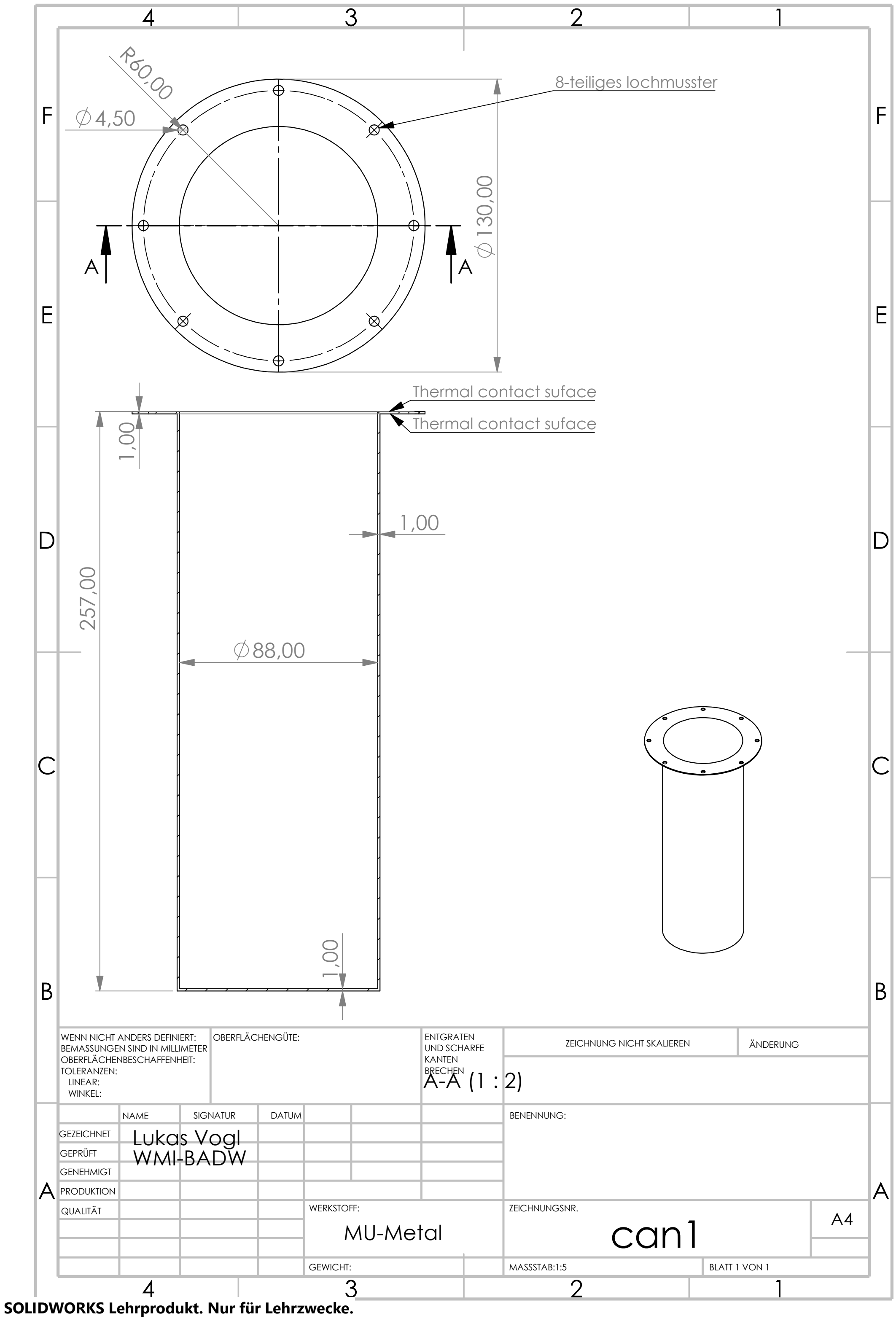

R60,00
⌀4,50
8-teiliges lochmusster
⌀130,00
A
A
Thermal contact suface
Thermal contact suface
1,00
1,00
257,00
⌀88,00
1,00
WENN NICHT ANDERS DEFINIERT: BEMASSUNGEN SIND IN MILLIMETER OBERFLÄCHENBESCHAFFENHEIT: TOLERANZEN: LINEAR: WINKEL:
OBERFLÄCHENGÜTE:
ENTGRATEN UND SCHARFE KANTEN BRECHEN
ZEICHNUNG NICHT SKALIEREN
ÄNDERUNG
A-A (1 : 2)
NAME
SIGNATUR
DATUM
BENENNUNG:
GEZEICHNET
Lukas Vogl
GEPRÜFT
WMI-BADW
GENEHMIGT
PRODUKTION
QUALITÄT
WERKSTOFF:
MU-Metal
ZEICHNUNGSNR.
can1
A4
GEWICHT:
MASSSTAB:1:5
BLATT 1 VON 1
SOLIDWORKS Lehrprodukt. Nur für Lehrzwecke.

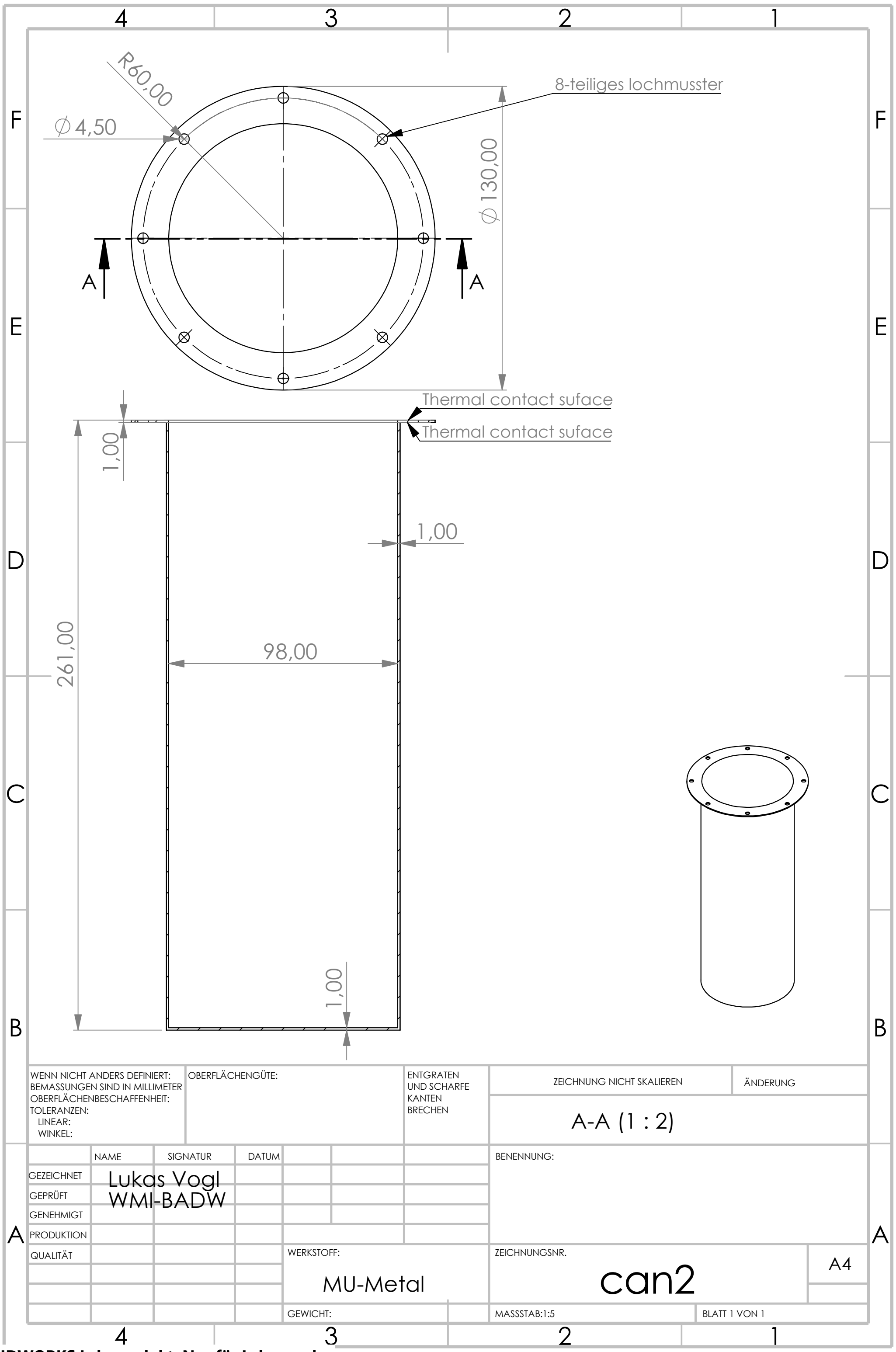

SOLIDWORKS Lehrprodukt. Nur für Lehrzwecke.

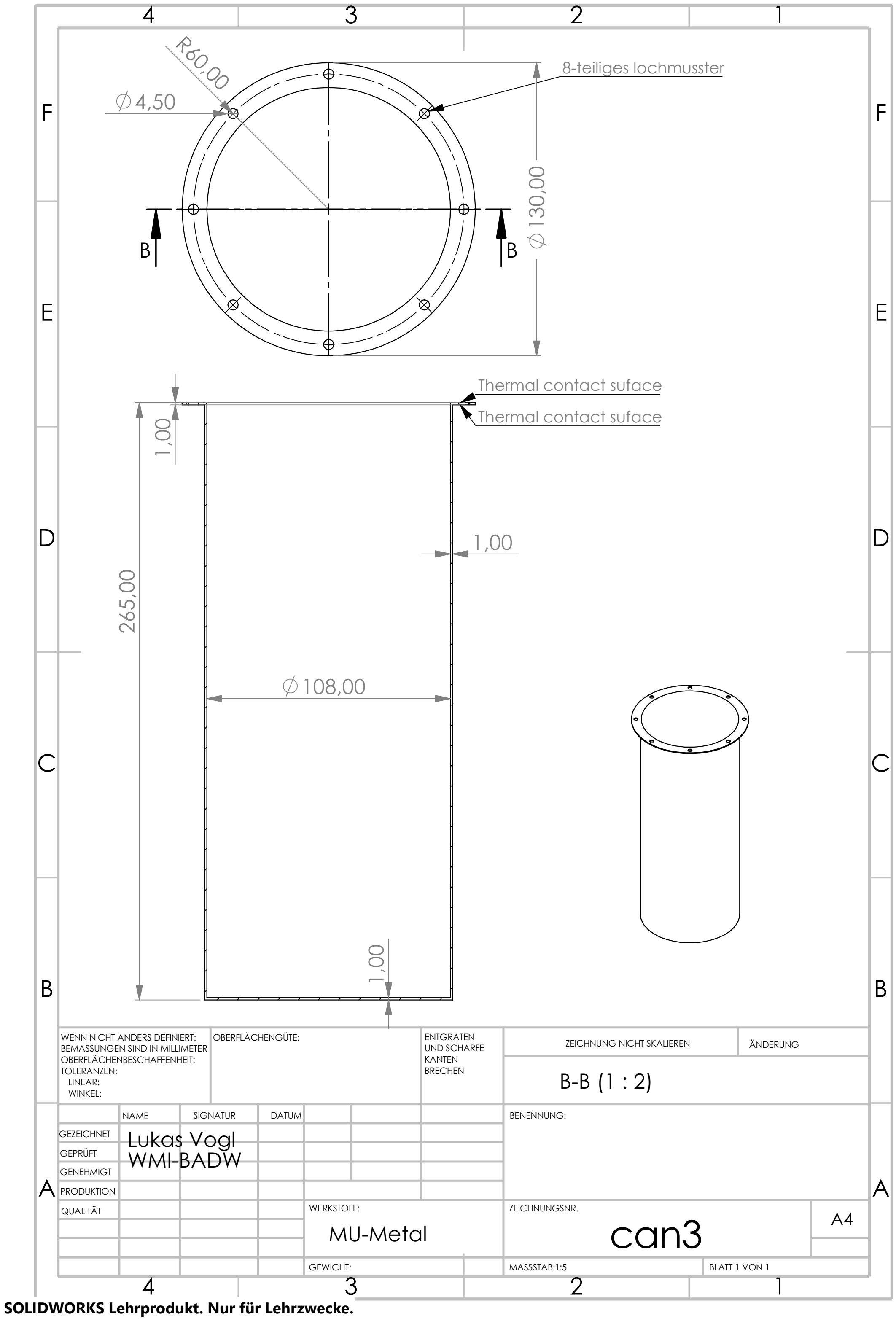
R60,00
∅4,50
8-teiliges lochmusster
∅130,00
B
B
Thermal contact suface
Thermal contact suface
1,00
1,00
265,00
∅108,00
1,00
WENN NICHT ANDERS DEFINIERT:
BEMASSUNGEN SIND IN MILLIMETER
OBERFLÄCHENBESCHAFFENHEIT:
TOLERANZEN:
LINEAR:
WINKEL:
OBERFLÄCHENGÜTE:
ENTGRATEN UND SCHARFE KANTEN BRECHEN
ZEICHNUNG NICHT SKALIEREN
ÄNDERUNG
B-B (1 : 2)
NAME
SIGNATUR
DATUM
BENENNUNG:
GEZEICHNET
GEPRÜFT
GENEHMIGT
PRODUKTION
QUALITÄT
Lukas Vogl
WMI-BADW
WERKSTOFF:
MU-Metal
ZEICHNUNGSNR.
can3
A4
GEWICHT:
MASSSTAB:1:5
BLATT 1 VON 1
SOLIDWORKS Lehrprodukt. Nur für Lehrzwecke.

List of Figures

List of Tables

Bibliography

[1] P. Arpaia, P. N. Burrows, M. Buzio, C. Gohil, M. Pentella, and D. Schulte. "Magnetic characterization of Mumetal® for passive shielding of stray fields down to the nano-Tesla level." In: *Nuclear Instruments and Methods in Physics Research Section A: Accelerators, Spectrometers, Detectors and Associated Equipment* 988 (2021), p. 164904. ISSN: 0168-9002. DOI: `https://doi.org/10.1016/j.nima.2020.164904`.

[2] *Bluefors xld dilution refrigerator*. `https://bluefors.com/products/xld-dilution-refrigerator/`. Online, accessed 10.07.2022.

[3] *Cryophy Data Sheet*. `https://www.aperam.com/sites/default/files/documents/CRYOPHYOCT2022V1EN.pdf`. Online, accessed 06 December 2022. October 2022.

[4] K. I. Gerasimov, M. M. Minnegaliev, B. Z. Malkin, E. I. Baibekov, and S. A. Moiseev. "High-resolution magneto-optical spectroscopy of $^{7}LiYF_4 :^{167} Er^{3+}$, $^{166}Er^{3+}$ and analysis of hyperfine structure of ultranarrow optical transitions." In: *Phys. Rev. B* 94 (5 Aug. 2016), p. 054429. DOI: `10.1103/PhysRevB.94.054429`.

[5] P. Granum, M. L. Madsen, J. T. K. McKenna, D. L. Hodgkinson, and J. Fajans. "Efficient calculations of magnetic fields of solenoids for simulations." In: *Nuclear Instruments and Methods in Physics Research Section A: Accelerators, Spectrometers, Detectors and Associated Equipment* 1034 (2022), p. 166706. ISSN: 0168-9002. DOI: `https://doi.org/10.1016/j.nima.2022.166706`.

[6] D. J. Griffiths. *Introduction to Electrodynamics: Pearson New International Edition*. Harlow, UNITED KINGDOM: Pearson Education UK, 2013. ISBN: 9781292034652.

[7] *Helmholtz-Spule*. `https://de.wikipedia.org/wiki/Helmholtz-Spule`. online, accessed 03.05.2023.

[8] L. Liu. *How the B-H Curve Affects a Magnetic Analysis (and How to Improve It)*. `https://www.comsol.com/blogs/how-the-b-h-curve-affects-a-magnetic-analysis-and-how-to-improve-it/`. Online, accessed 07 December 2022. 26 November 2019.

[9] NOAA. *Magnetic Field Calculators*. `https://www.ngdc.noaa.gov/geomag/calculators/magcalc.shtml`. Online, accessed 20.02.2023.

[10] C. Simon, M. Afzelius, J. Appel, A. Boyer de la Giroday, S. J. Dewhurst, N. Gisin, C. Y. Hu, F. Jelezko, S. Kröll, J. Müller J. H. and Nunn, E. S. Polzik, J. G. Rarity, H. De Riedmatten, W. Rosenfeld, A. J. Shields, N. Sköld, R. M. Stevenson, R. Thew, I. A. Walmsley, M. C. Weber, H. Weinfurter, J. Wrachtrup, and R. J. Young. "Quantum memories." In: *The European Physical Journal D* 58.1 (May 2010), pp. 1–22. ISSN: 1434-6079. DOI: `10.1140/epjd/e2010-00103-y`.

[11] A. e. a. Strinic. “in preparation.” In: (2023).

[12] T. L. Tang. *Finite length Solenoid potential and field*. https://nukephysik101.files.wordpress.com/2021/07/finite-length-solenoid-potential-and-field-1.pdf. Online, accessed 10.03.2023.

[13] *Using PPMS Suerconducting Magnets at Low Fields*. https://qdusa.com/sideDocs/appNotes/1070-207.pdf. online, accessed 27.04.2023.

[14] Y. Wiemann, J. Simmendinger, C. Clauss, L. Bogani, D. Bothner, D. Koelle, R. Kleiner, M. Dressel, and M. Scheffler. “Observing electron spin resonance between 0.1 and 67 GHz at temperatures between 50 mK and 300 K using broadband metallic coplanar waveguides.” In: *Applied Physics Letters* 106.19 (May 2015). 193505. ISSN: 0003-6951. DOI: 10.1063/1.4921231. eprint: https://pubs.aip.org/aip/apl/article-pdf/doi/10.1063/1.4921231/14320308/193505_1_online.pdf.

[15] M. Zhong, M. P. Hedges, R. L. Ahlefeldt, J. G. Bartholomew, S. E. Beavan, S. M. Wittig, J. J. Longdell, and M. J. Sellars. “Optically addressable nuclear spins in a solid with a six-hour coherence time.” In: *Nature* 517.7533 (Jan. 2015), pp. 177–180. ISSN: 1476-4687. DOI: 10.1038/nature14025.

Acknowledgments

I want to thank here every body who enabled me to do this work.
Special thanks to:

Prof. Dr. Rudolf Gross for providing the possibility for working at WMI and his passion for teaching.

Dr. Nadezhda Kukharchyk for the close mentorship over the last year and for providing the topic for this thesis.

Ana Strinic for all the help and support in the lab during the measurements and during the analysis process. As well for providing the reference data.

The rest of the mw-RESystem group, Georg, Owen, Chiun and Jianpeng for the teamwork and pleasant talks during lunch.

Gerhard Huber for the joint measurement and his insights about his setup.

The WMI-workshop for the great help in the design and building phase and the very fast building time.

And at last but definitely not least, I want to thank my Family for keeping up with me and keep me motivated, thank you very much.